Chapter 3

New Particle Formation from Photooxidation of Diiodomethane (CH_2I_2)*

* This chapter is reproduced by permission from "New Particle Formation from Photooxidation of Diiodomethane (CH_2I_2)" by J.L. Jimenez, R. Bahreini, D.R. Cocker, H. Zhuang, V. Varutbangkul, R.C. Flagan, J.H. Seinfeld, T. Hoffmann, C. O'Dowd, *Journal of Geophysical Research-Atmosphere*, 108 (D10), 4318, doi:10.1029/2002JD002452, 2003 and *Journal of Geophysical Research-Atmosphere*, *108* (D23), 4733, doi:4710.1029/2003JD004249, 2003.

3.1. Abstract

Photolysis of CH_2I_2 in the presence of O_3 has been proposed as a mechanism leading to intense new particle formation in coastal areas. We report here a comprehensive laboratory chamber study of this system. Rapid homogeneous nucleation was observed over three orders of magnitude in CH_2I_2 mixing ratio, down to a level of 15 ppt (~4 x 10^8 molec. cm^{-3}), comparable to the directly measured total gas-phase iodine species concentrations in coastal areas. After the nucleation burst, the observed aerosol dynamics in the chamber was dominated by condensation of additional vapors onto existing particles and particle coagulation. Particles formed under dry conditions are fractal agglomerates with mass fractal dimension, D_f ~ 1.8-2.5. Higher relative humidity (65%) does not change the nucleation or growth behavior from that under dry conditions, but results in more compact and dense particles (D_f ~2.7). Based on the known gas-phase chemistry, OIO is the most likely gas-phase species to produce the observed nucleation and aerosol growth, however the current understanding of this chemistry is very likely incomplete. Chemical analysis of the aerosol using an Aerodyne Aerosol Mass Spectrometer reveals that the particles are composed mainly of iodine oxides, but also contain water and/or iodine oxyacids. The system studied here can produce nucleation events as intense as those observed in coastal areas. Based on comparison between the particle composition, hygroscopicity, and nucleation and growth rates observed in coastal nucleation and in the experiments reported here, it is likely that photooxidation of CH_2I_2-- probably aided by other organic iodine compounds-- is the mechanism leading to the observed new particle formation in the west coast of Ireland.

3.2. Introduction

Homogeneous nucleation is a source of new particles in the atmosphere. New particle formation has been observed in regions that have undergone cloud processing, forested areas, polluted air masses, the marine boundary layer, Arctic areas, and coastal regions. In some instances, observed atmospheric new particle formation is consistent with binary homogeneous nucleation of sulfuric acid and water, while in others, an additional mechanism needs to be invoked, probably ternary homogeneous nucleation of sulfuric acid, ammonia, and water [*Weber et al.*, 1999; *Kulmala et al.*, 2002].

Coastal zones have been known to be a locus of significant new particle formation for more than a century [*Aitken*, 1897], but the study of this phenomenon has intensified only recently [*O'Dowd et al.*, 1998, 1999, 2002; *Grenfell et al.*, 1999]. Evidence points to gaseous alkyl iodides as precursors to particle production in this environment [*Laturnus,* 1996; *Alicke et al.*, 1999; *Carpenter et al.*, 1999; *Cox et al.*, 1999]. The 1998-99 PARFORCE campaign [*O'Dowd et al.*, 2002], conducted on the west coast of Ireland, is the most intensive field study of coastal new particle formation to date. Nucleation was observed at this location on most days, for all seasons, and all air masses. Aerosols formed by this mechanism are estimated to significantly increase both direct scattering and CCN concentrations. Observations at this location point to the possible role of diiodomethane (CH_2I_2) in the measured new particle formation.

CH_2I_2 is the most abundant of the measured iodine-containing compounds released by macroalgae [*Mákelá et al.*, 2002] and appears to be the most important compound controlling the influx of iodine atoms into the coastal boundary layer [*Carpenter et al.*, 1999]. CH_2I_2 is rapidly photolyzed by sunlight reaching the Earth's surface. Several

studies have developed gas-phase atmospheric oxidation mechanisms for iodine species [*Sander et al*., 1997; *Vogt et al.*, 1999; *McFiggans et al.*, 2000], but the molecular routes leading to new particle formation and particle growth have not been unequivocally established. The evidence pointing to the role of CH_2I_2 in the observed nucleation included: a) CH_2I_2 and IO (the latter is produced from CH_2I_2) showed coherence with the tidal cycle, which in turn, was strongly correlated with the nucleation events; b) solar radiation was also needed for nucleation to occur, which is consistent with a mechanism based on CH_2I_2 photolysis; c) iodine was always observed in the nucleation mode particles, while sulfur was detected only some of the time, and chlorine or bromine were never present; d) ultrafine particle hygroscopic growth factors indicated very low solubility, which rules out sulfate aerosol; e) neither H_2SO_4, VOCs, nor any species associated with polluted air masses can explain the observed nucleation and growth.

Kulmala et al. [2002] conclude from a modeling study that new particle formation from ternary nucleation of H_2SO_4-NH_3-H_2O could have occurred almost continuously during PARFORCE, but there was insufficient vapor phase H_2SO_4 to grow the particles to observable sizes. They suggest that while the new particle formation may be due to H_2SO_4-NH_3-H_2O, another species is responsible for the growth of these particles to detectable sizes, thus decoupling the nucleation and particle growth mechanisms. If the condensing species cannot nucleate on its own, new particle formation may not occur at other coastal areas where the same condensable species are present, if the H_2SO_4-NH_3-H_2O system does not provide the initial nuclei.

On the basis of laboratory experiments, *Hoffmann et al.* [2001] demonstrated that rapid particle formation occurs after photolysis of CH_2I_2 in the presence of O_3. Based on

measurements of the chemical composition of particles formed, these authors suggested that self-nucleation of iodine dioxide (OIO) may be an effective mechanism of new particle formation in coastal regions. However; their experimental set up was not well suited for a quantitative study of this system.

Laboratory chamber experiments provide the ability to study aerosol nucleation and growth under well-controlled conditions of temperature, humidity, pre-existing particles, precursor gas-phase concentrations, and radiation [*Cocker et al.*, 2001]. Following the work of *Hoffmann et al.* [2001], we present here a comprehensive quantitative laboratory chamber investigation of particle formation from photolysis of CH_2I_2 in the presence of ozone. Measurements are carried out on particle formation and growth under both dry and moderately humid conditions, as well as on the hygroscopicity and chemical composition of the aerosols produced. The goals of this work are to characterize the chemical routes leading to new particles, the rates of particle formation and growth, the properties of the aerosols formed, and to evaluate whether this mechanism could be responsible for the strong nucleation events observed in the PARFORCE campaign. In Section 3.2, we describe the experimental system, including the laboratory chamber facility, and the instrumentation for particle number, size, composition, and hygroscopicity measurement. The experimental observations are summarized in Section 3.3, while a detailed interpretation of the size distribution measurements is presented in Section 3.4. Section 3.5 describes the results of a detailed gas-phase and aerosol uptake model for the chamber, and compares the results of the model with the experimental data. Finally, section 3.6 provides an integrated interpretation of the data in terms of the

aerosol chemistry, and section 3.7 compares the results of this study with those of the PARFORCE field study.

3.3. Experimental Description

Aerosol formation from the direct photolysis of CH_2I_2 in the presence of O_3 was investigated in the Caltech indoor chamber. This facility has been described in detail previously [*Cocker et al.*, 2001]. Briefly, the Caltech indoor facility consists of dual, 28 m^3 chambers illuminated by 300 1.22 m fluorescent blacklights (Sylvania 350BL), which are used to simulate the UV and near UV regions of ambient sunlight [*Carter et al.*, 1995]. The UV and visible light intensity was measured with a portable spectroradiometer (LI-1800, LI-COR, Lincoln, Nebraska), which had been calibrated at the factory immediately before these measurements. The UV intensity at the peak of 354 nm was 2.9 W m^{-2} nm^{-1}, with the relative spectral dependence described in *Cocker et al.* [2001]. The estimated photolysis rate of NO_2 was 0.6 min^{-1}. This is in good agreement with previous measurements in this chamber for aged lights, and corresponds to about 1.2 times the maximum rate at the Earth's surface with a solar zenith angle of 0^o. The reaction chamber was originally filled with clean dry air at 1 atm and 20^oC. Air temperature inside the chamber and surrounding the equipment and the sample lines was maintained at $20^oC \pm 2^oC$. A dilute solution of CH_2I_2 in C_6F_6 was prepared and injected into a glass flask with a microliter syringe. The solution was evaporated and introduced into the bag by flowing clean particle-free dry air over the solution on the flask, and aiding the process with slight heating. For humid experiments, water vapor was injected into the chamber to reach the desired RH of 65% ± 5 %. For dry experiments, RH was less than 2% ± 1%, below the detection limit of the available hygrometer. Initial ozone

mixing ratios were 100 ppb ± 20 ppb. The UV lights were turned on after all components were well mixed in the chamber. Repetition of some experiments indicated a reproducibility of ± 15% or better. This level of reproducibility is not as good as that achieved for secondary organic aerosol formation experiments conducted previously in the same facility. A possible explanation may be derived from our experimental observation that CH_2I_2 (and probably some of its reaction products as well) is a "sticky" substance, i.e., it has a significantly greater tendency to attach to surfaces, such as injection lines and chamber walls, than the non-halogenated organics involved in secondary organic aerosol studies.

3.3.1. CH_2I_2 (Surrogate) Concentration Measurement

An FID gas chromatograph (GC, Hewlett Packard, Model 5890, Series II) was used to check the initial concentration of CH_2I_2 after injection of this species before beginning each experiment. Since CH_2I_2 would not elute on the capillary column in the GC, which was optimized for analysis of non-polar or slightly polar hydrocarbons, the GC was used to measure the concentration of C_6F_6 as a surrogate of the CH_2I_2 concentration. The GC was calibrated by preparing known gas-phase C_6F_6 concentrations by injecting known amounts of C_6F_6 into a small Teflon bag, and then sampling the small bag into the GC. The actual concentration of CH_2I_2 in the chamber was deduced from monitoring the response of the GC to C_6F_6 in the beginning of each experiment (before the UV lights were switched on) and using the calibration equation. The CH_2I_2 concentration estimated in this manner was on average –8% ± 4% of the concentration predicted from the amount of solution injected, the solution concentration, and the volume of the chamber.

3.3.2. Particle Number and Size Distribution Measurements

Particle size distributions were measured by a scanning electrical mobility spectrometer (SEMS) [*Wang and Flagan,* 1989]. The SEMS is equipped with a TSI model 3077 ^{85}Kr neutralizer (TSI Inc., St. Paul, MN), a long column cylindrical differential mobility analyzer (TSI 3071), and a condensation particle counter (CPC, TSI 3760). The DMA was operated with sheath and excess flows of 2.5 LPM, and polydisperse and monodisperse flows of 0.25 LPM. By changing the voltage of the DMA exponentially between –30 and –7000 V, a mobility spectrum was obtained every 90 s over particle diameters ranging from 25 nm to 700 nm.

Newly formed particles from homogeneous nucleation have diameters less than 25 nm, below the detection limit of the SEMS as operated in this study. Moreover, the number concentrations of nucleated particles may exceed the maximum concentrations and change faster than this SEMS can measure. For these reasons, independent particle number concentrations were recorded using a TSI CPC 3025 and a TSI CPC 3010. The detection efficiencies of these CPCs are 50% for particles of 3 and 10 nm, respectively [*TSI*, 1996; *Hämeri et al.*, 2002]. The smallest detectable particles are about 2 nm and 6 nm for the CPC 3025 and 3010, respectively [*Hämeri et al.*, 2002]. Particle coincidence in the CPCs was minimized by diluting the sampled aerosol stream by a factor of 1000. This extended the measurement range up to 10^7 and 10^8 cm^{-3} for the CPC 3010 and CPC 3025, respectively. The detection efficiencies of the CPC 3025 as operated here are estimated at 0.17%, 8.4%, 30%, and 88% for particles of sizes 3, 6, 10, and 50 nm, respectively. The low detection efficiencies at the small size limit are due to diffusion losses in the tubing from the point of sampling, through the dilution system, to

the CPC, and, to a lesser extent, to the lower efficiency of the CPC itself for small particle sizes [*Hinds*, 1999; *Hämeri et al.*, 2002]. In the first moments after nucleation starts in the chamber, the CPC 3010 does not detect any particles while the CPC 3025 does. Given the size detection limits of both CPCs and the detection efficiency of the CPC 3025 at those sizes, we estimate that the concentrations reported by the CPC 3025 during this initial phase should be multiplied by a factor between 12 and 600 to determine the actual concentration. Due to the large uncertainties in the detection efficiencies, all the CPC data are presented here without correction (as recorded).

3.3.3. Aerosol Mass Spectrometer (AMS)

An Aerodyne Aerosol Mass Spectrometer [*Jayne et al.*, 2000; *Jimenez et al.*, 2002] was used to simultaneously monitor particle vacuum aerodynamic diameter and chemical composition. The AMS uses an aerodynamic lens to focus the particles into a narrow beam that is then introduced into a high vacuum chamber while the air is differentially pumped. Volatile and semi-volatile species in/on the particles are vaporized on a heated, roughened molybdenum surface under high vacuum (10^{-7} Torr) at about 600°C. The vaporized species are then ionized by the impact of energetic electrons (70 eV). The ions formed are analyzed by a quadrupole mass spectrometer (QMA 430, Balzers Instruments, Balzers, Liechtenstein). Particle aerodynamic size is determined via particle time-of-flight, with the starting time provided by the opening time of a rotating beam chopper and the arrival time by the chemical detection. The AMS can produce two types of data: mass spectra of the species present in/on the aerosol, without size information; and mass-weighed size distributions vs. vacuum aerodynamic diameter ($dM/d\log D_{va}$) of the aerosol at a series of *m/z* peaks of the mass spectrometer.

3.3.4. Hygroscopicity Tandem Differential Mobility Analyzer (HTDMA)

A hygroscopicity tandem differential mobility analyzer (HTDMA) was used to measure the response of the aerosol to changes in relative humidity. The HTDMA, based on the original design of *Rader and McMurry* [1986], consists of a ^{85}Kr neutralizer, a fixed voltage long column differential mobility analyzer (DMA model 3081, TSI Inc.) used to select a narrow size range of chamber aerosol (under the humidity of the chamber), a cylindrical laminar flow chamber for aerosol humidification or dehumidification, followed by a second scanning long column DMA (TSI model 3081) and condensation particle counter (CPC model 3760A, TSI Inc.) operated as a SEMS [*Cocker et al.*, 2001]. This SEMS performed one full particle size scan every 75 s, while the sizes selected by the first DMA and/or the final humidity were changed every ~10 min. Flow rates of 2.5 LPM were used for both sheath and excess flows, and 0.25 LPM for both polydisperse and monodisperse aerosol flows. The classified aerosol was introduced on the centerline of the humidification chamber to minimize variations of residence time (10 s for the flow and configuration used). The data inversion algorithm used is described by *Collins et al.* [2002].

3.3.5. Summary of Experiments Performed

Table 3.1 summarizes the experiments carried out. We have chosen a base case (E1) with initial conditions of 5 ppb CH_2I_2, 100 ppb O_3, and RH < 2%. The effect of relative humidity was investigated with experiment E2, which is similar to E1 except for RH = 65%. The effect of the initial CH_2I_2 concentration was investigated with four additional experiments at 500 ppt (E3), 50 ppt (E4), 15 ppt (E5), and 50 ppb (E6). The effect of UV radiation intensity was investigated with experiment E7. Finally, experiments E8 and E9

were conducted to investigate whether particles form in the absence of UV light or O_3, respectively.

3.4. Experimental Observations

3.4.1. Particle Formation and Growth

Photolysis of CH_2I_2 in the absence of O_3 does not lead to particle formation; likewise, no particles form in mixtures of CH_2I_2 and O_3 in the dark. Particle production requires both photolysis of CH_2I_2 and the presence of O_3. Homogeneous nucleation was observed after inception of photolysis of CH_2I_2/O_3 mixtures under both dry and humid conditions and for all CH_2I_2 concentrations tested. Figure 3.1 illustrates the general behavior of aerosol number and volume concentrations over the course of the base case experiment (E1). Particle concentrations measured in the first few minutes are shown in Figure 3.2. A burst of new particle formation occurred ~30 s after the inception of photolysis. The newly formed particles are first detected by the CPC 3025, but not by the CPC 3010, SEMS, or AMS, which indicates that their size is at least 2 nm, but less than 6 nm. As the reaction proceeded, the particle number reached a peak at about 100 s after the inception of photolysis and then rapidly decayed. Subsequent detection of the particles by the CPC 3010, SEMS, and AMS shows that significant numbers of these particles started to grow to 10 nm or larger about after 1 min of photolysis, and to 25 nm or larger after 3 min. This growth can result from uptake of gas-phase species by the existing particles and/or from particle coagulation. Additional brief nucleation bursts were observed after the initial burst during some experiments, likely as a result of a buildup of the nucleating species due to slow removal by condensation on existing particles, as described

previously for other smog chamber studies of secondary aerosol formation [*Flagan et al.*, 1991].

A difference in measured number concentrations with the CPCs detecting a higher number than the SEMS persisted for about 50 minutes after inception of photolysis, indicating that significant new particle formation lasted for, at most, that long. The processes controlling the aerosol dynamics immediately following the number concentration peak can be estimated from the time scales of decay: e-folding time of decay $\tau \sim$ 12 min for CPC 3025 and ~ 19 min. for CPC 3010. The time scales of coagulation and wall loss for 3 nm particles at that time are estimated as 39 min and 10 min, while for 10 nm particles they are 29 min and 33 min. Thus, wall loss is dominant for 3 nm particles, while both processes are equally important for 10 nm particles. These time scales suggest that nucleation could have ended before 50 min, and that the remaining small particles observed up to that time simply did not have enough time to grow by condensation or coagulation. However, it is not possible to determine from the available data when nucleation actually ended.

SEMS size distributions of the particles produced during the photooxidation are shown in Figure 3.3. Particles grow into the SEMS size range in significant numbers about 5 min after the start of photolysis. These particles grow rapidly, forming a distinct large particle mode at about 8 min. after the start. Rising concentrations for the smaller particles of the size distribution reveal a second mode at sizes too small to resolve with the SEMS. The persistence of this fine particle mode for 50 min reinforces the previous observation from the CPC data that new particle formation continued for at most that time into the experiment. The population of the large SEMS mode first increases and then

decreases, while its mode size increases continuously with time. The mode of the number distribution grows from the smallest detectable value of 25 nm to about 100 nm after 2 h, and 170 nm after about 6 h.

The AMS provides an independent measurement of the aerosol mass distribution vs. vacuum aerodynamic diameter ($dM/d\log D_{va}$) at each *m/z* with a detectable signal. Figure 3.4 compares the volume and mass distributions measured for the base case by the SEMS and the AMS. The general behavior in time of the AMS mass distribution is similar to that of the volume distribution calculated from the SEMS data. However, two significant differences are observed: the size distribution measured by the AMS is narrower than that measured by the SEMS; and the growth of the mass mode as detected in the AMS slows down considerably after about 1 h, while the SEMS indicates continued growth of the mobility diameter mode. These differences between the mobility and vacuum aerodynamic diameter measurements of the SEMS and the AMS are used below to estimate particle effective density. The reason for the broader size distribution on the SEMS as compared to the AMS may be due to the particles being fractal agglomerates (see section 3.4). The particles spend a much longer time inside the SEMS column while being size-classified (seconds) than in the AMS expansion that imparts them a size-dependent velocity (< 1 ms). Under these circumstances, it is likely that the diffusional broadening of the distribution due to particle shape is greater in the SEMS due to the longer time available.

The total aerosol volume concentration was obtained from the SEMS size distributions (assuming dense spherical particles), while a signal proportional to aerosol mass was obtained from the AMS; both are also shown in Figures 3.1 and 3.2. Since total

particle volume is dominated by the largest particles, once about half of the particles have grown above the SEMS detection limit of 25 nm mobility diameter (t > 20 min), the error due to the volume of particles below this limit diminishes rapidly. The particle volume increased with $\tau \sim 45$ min, much more slowly than the particle number concentration, and reached a maximum value of about 85 $\mu m^3\ cm^{-3}$ after about 150 min. The particle mass concentration measured by the AMS starts to rise a few minutes earlier than the SEMS volume, an observation that is exploited in section 3.4.1 to determine the effective density of the particles detected at this time. Later, the evolution of the AMS aerosol mass signal is close to that of the volume calculated from the SEMS data for about 80 min, but it levels off earlier than the SEMS volume. After nucleation ceased, the observed increase in particle volume and mass is a result of condensation of additional vapors onto the existing particles. The later discrepancy between the SEMS and AMS may indicate that while condensation has ended after about 80 min, the apparent particle volume still increases due to the production of agglomerate particles by coagulation.

The main results of the parametric experiments are summarized in Table 3.1. The effect of relative humidity on the particle formation process was investigated with an experiment identical to the base case except for the moderately humid condition (RH = 65%, Exp. E2). No significant difference was observed in the nucleation delay, initial particle number burst, the shape of the particle volume and mass vs. time, or the shape of the SEMS and AMS size distributions compared to those of the dry case. The main difference is that the apparent particle volume (assuming dense spherical particles) calculated from the SEMS data for the humid experiment is about half of that of the dry experiment. Although the number concentrations and the shape of the size distribution

are similar under both conditions, the mobility diameter of the particles is smaller under humid conditions, resulting in the observed difference in the volume. The vacuum aerodynamic diameter mode measured by the AMS, however, is larger than for the dry case. Both of these observations suggest that the particles are more dense and compact in the humid experiment than in the dry experiment, an issue that is explored further in section 3.4.

Varying the initial concentration of CH_2I_2 over more than three orders of magnitude did not qualitatively change the observed phenomena. A burst of new particle formation followed by a decrease in particle number with increasing particle size and volume was observed for all CH_2I_2 levels. The maximum number, area, and volume concentrations of the aerosol formed increase with increasing CH_2I_2 concentration, as shown in Figure 3.5, although the increase is less than linear (approximately proportional to $[CH_2I_2]^{0.65}$ to $[CH_2I_2]^{0.85}$). The most significant difference from the base case is that the time scales of all processes (delay before initial nucleation burst, particle number growth, and volume growth) increased substantially with decreasing initial CH_2I_2 concentration, as shown in Figure 3.6. The change in time scale is well approximated by a power law dependence, with the time scale being proportional to $[CH_2I_2]^{-0.43}$ for the nucleation delay, $[CH_2I_2]^{-0.63}$ for the time to number peak, and $[CH_2I_2]^{-0.37}$ for the volume growth. For the lowest CH_2I_2 concentration (E5), the time scale of particle volume growth was about 8 h, and consequently its dynamics in the chamber are significantly affected by particle (and probably gas) loss to the chamber walls.

Varying the intensity of the UV radiation (E7) to ¼ of the base case increased the nucleation delay, the time to reach the peak of particle number concentration, and the

time scale of aerosol volume by factors of 1.5, 2.4, and 2.7, respectively. The amount of aerosol formed was very similar to that of the base case.

3.4.2. Hygroscopic Properties

The HTDMA was used to measure the hygroscopic growth factor (G_f) of the iodine aerosol, which is defined as the ratio of the aerosol electrical mobility diameter after humidification (or drying) to that prior to humidification. Figure 3.7 shows G_f for the aerosol produced from the photooxidation of CH_2I_2. For the aerosol formed in the base case dry experiment (E1), increasing RH up to approximately 20% has no effect on the electrical mobility diameter. Beyond 23% RH, G_f starts to decrease, indicating that the mobility diameter of the particles is shrinking as RH increases. At ~55% RH, G_f reaches a minimum value of 0.66. For most experimental systems, aerosol growth factors for increasing RHs are equal to or exceed 1.0, i.e., either the particles do not change size or they grow by water uptake. We cannot rule out that the particles lose some mass upon interaction with increasing water vapor, and in fact, gaseous I_2 has been observed to evolve from aerosol formed in dry flowtube experiments for a related chemical system after exposure to ambient air [*Milligan*, 2002]. More likely, however, the particles formed under dry conditions are not compact. The increase in water partial pressure appears to promote rearrangement of these low-density structures, resulting in a smaller mobility equivalent diameter. *Weingartner et al.* [1997] observed similar behavior during HTDMA experiments with fractal carbon particles produced in a spark discharge between two graphite electrodes. They attributed the observed decrease in mobility diameter of their particles after exposure to water vapor to preferential water condensation in small angle cavities of the particles, due to the inverse Kelvin effect,

leading to capillary forces on the aggregate branches that cause them to collapse. We speculate that a similar effect may be causing the particle diameter reduction observed here. In our system, the mobility diameter eventually rises after further increase in RH, suggesting that additional water uptake causes the particles to grow. The upward trend continues to the 85% maximum RH studied. Therefore, after the initial compaction, at least one component of the aerosol is hydrophilic, leading to an increase in size with increasing RH.

In contrast to the dry experiment, the aerosol formed in the humid experiment (E2) shows little tendency to change its mobility diameter when exposed to variable water vapor concentration up to RH = 75%. At higher relative humidities, the larger particles shrink, suggesting that the additional humidity promoted further consolidation of the particles. The reason why the particles formed under humid conditions do not show the same growth at high RH as the particles formed under dry conditions is unclear.

3.4.3. Particle Composition

Figure 3.8 shows a total aerosol mass spectrum obtained with the AMS for the highest concentration experiment (E6). The detected *m/z* peaks can be assigned to O^+, OH^+, H_2O^+, I^{2+}, I^+, HI^+, IO^+, HIO^+, IO_2^+, HIO_2^+, HIO_3^+, IO_5^+, I_2^+, I_2O^+, and $I_2O_3^+$. IO_3^+ and IO_4^+ are not observed within the detection limit of the AMS. We also observe the peaks for MoO^+ and MoO_2^+, characterized by the distinct isotope pattern of Mo. The Mo-containing ions must originate from the reaction of the particle material with the AMS vaporizer, which is made of molybdenum. Acid halides, which may be present in the particles, are known corrosive agents [*Behrens et al.*, 1989]. *Hoffmann et al.* [2001] report the detection of I^-, IO^-, IO_2^-, IO_3^-, and I_2^- from particles produced in a similar

experiment using a chemical ionization mass spectrometer after vaporization in N_2/air at 550°C. They do not report any hydrogen-containing species. The relative aerosol signals measured by the AMS at the different *m/z* peaks were independent of time in the experiment as well as of particle size. Since the AMS detected particles as small as about 20 nm (physical diameter), this indicates that the particle composition was homogeneous and that the species responsible for initial nucleation and growth were likely the same as those comprising most of the particles at later times (although the ~1-3 nm particles formed during the initial nucleation burst are too small for detection with the AMS used here). Relative humidity of 65% was found to increase the signals at OH^+ and H_2O^+ by a factor of five, while the signals at HI^+, HIO^+, HIO_2^+, and HIO_3^+ were about only half as intense as in the dry case. Implications of these results are discussed below.

Other minor peaks were also detected at *m/z* 28, 30, 44, 190, and 221. The first two peaks were about 100 times less intense than the base peak (I^+) and may correspond to CO^+, CH_2O^+, and CO_2^+, resulting from a small amount of formaldehyde or other oxidized organics partitioning onto the aerosol. These organics must originate from reactions of the carbon-containing products of CH_2I_2 photolysis. The later two peaks, which are about 1000 times less intense than the base peak, would be consistent with the ions $HIO_3CH_2^+$ and $IO_5CH_2^+$.

3.5. Interpretation of Size Distribution Observations

3.5.1. Estimates of Particle Effective Density

An effective particle density can be derived by comparing the particle size measurements performed by the SEMS and the AMS. In this section, we first introduce

the physical basis for the dependence of both size measurements on particle density and shape, and later derive particle effective densities for our chamber experiments.

The SEMS measures the electrical mobility of the particle, leading to an estimation of the mobility-equivalent diameter. The electrical mobility of a particle, Z_p, is the ratio of the steady-state migration velocity to the applied electric field, and it is proportional to the particle charge and inversely proportional to the drag force acting on the particle. The electrical mobility and the mobility equivalent diameter of a sphere are related by [*Flagan*, 2001]:

$$Z_p = \frac{neC_c(Kn)}{3\pi\eta D_p} \tag{1}$$

where n is the number of charges on the particle, e is the elementary unit of charge, C_c is the slip correction factor that accounts for non-continuum effects, Kn is the Knudsen number, η is the gas viscosity, and D_p is the physical diameter of the sphere. For particles of a given charge in the continuum regime $Z_p \propto D_p^{-1}$, while in the free molecular regime $Z_p \propto D_p^{-2}$. The Knudsen number is defined as

$$Kn = \frac{2\lambda}{D_p} \tag{2}$$

where λ is the mean free path of the gas molecules. Particles are considered to be in the free molecular regime for $Kn > 10$ and in the continuum regime for $Kn < 0.1$. At ambient pressure and temperature, $\lambda \sim 65$ nm, so that the particles measured by the SEMS are in the transition regime between free molecular and continuum conditions.

The mobility-equivalent diameter does not depend on the density of the particle material, but it does depend on particle shape. The drag force on a non-spherical particle migrating at a given velocity exceeds that of its volume-equivalent sphere by a factor χ,

known as the dynamic shape factor [*Fuchs*, 1964; *Baron and Willeke*, 2001]. The volume-equivalent diameter, D_v, is defined as the diameter of a sphere composed of the bulk particle material that has the same solid volume as the particle. It can be thought of as the diameter of the sphere that would result if the irregular particle melted to form a droplet [*Hinds*, 1999]. χ is equal to one for a sphere and larger than one for a non-spherical particle. The detailed relationship between particle physical shape (e.g., as determined with an electron microscope) and χ has only been studied for a limited range of particles and pressures (mostly ambient).

Using equation 1 we can relate the mobility-equivalent and volume-equivalent diameters as:

$$\frac{D_v \chi}{C_c\left(\frac{2\lambda}{D_v}\right)} = \frac{D_m}{C_c\left(\frac{2\lambda}{D_m}\right)} \tag{3}$$

In general the relationship between D_v and D_m needs to be determined numerically, due to the non-linear dependence of C_c on D_v and D_m. However it can be shown that the following approximate expression for C_c can be used with an error smaller than 10% for all Kn (for the values of α, β, and γ for solid or oil particles in *Baron and Willeke* [2001]):

$$C_c = 1 + Kn\left[\alpha + \beta \exp\left(-\frac{\gamma}{Kn}\right)\right] \approx 1 + (\alpha + 0.73\beta)Kn = 1 + \phi\, Kn \tag{4}$$

where $\phi = \alpha + 0.73\ \beta$. Substituting into Equation (3):

$$\frac{D_v \chi}{1 + \phi \frac{2\lambda}{D_v}} = \frac{D_m}{1 + \phi \frac{2\lambda}{D_m}} \tag{5}$$

which is quadratic in D_m, leading to:

$$D_m = \frac{D_v \chi}{2\left(1+\phi\frac{2\lambda}{D_v}\right)}\left[1+\sqrt{1+\frac{8\lambda\phi\left(1+\phi\frac{2\lambda}{D_v}\right)}{D_v\chi}}\right] = f(D_v, \chi, \lambda) \quad (6)$$

The AMS measures the particle aerodynamic diameter by determining their terminal velocity after expansion from a pressure of about 2 mbar into vacuum. The relationship between the aerodynamic diameter, D_a, and the volume-equivalent diameter is [*McMurry et al.*, 2002]:

$$D_a^2 C_c(D_a) = \frac{1}{\chi}\frac{\rho_p}{\rho_0} D_v^2 C_c(D_v) \quad (7)$$

where ρ_p is the density of the particle material, and ρ_0 is the unit density (1 g cm^{-3}). Because the mean free path at 2 mbar is about 33 μm, all submicron particles are in the free-molecular regime (Kn > 66) when acquiring a size-dependent velocity. Under these conditions we can approximate the slip correction factor as:

$$C_c(D) = 1 + Kn\left[\alpha + \beta\exp\left(-\frac{\gamma}{Kn}\right)\right] \approx (\alpha+\beta)Kn \quad (8)$$

which leads to the following expression for the relationship between aerodynamic diameter and volume-equivalent diameter on the free-molecular regime:

$$D_{va} = \frac{\rho_p}{\rho_0}\frac{D_v}{\chi_v} = \frac{\rho_p}{\rho_0}\chi_{v,inv} D_v = \frac{\rho_p}{\rho_0} S D_m \quad (9)$$

where D_{va} is the vacuum aerodynamic diameter, D_v is the volume equivalent diameter, D_m is the electrical mobility diameter, ρ_p is the density of the particle material, ρ_0 is the unit density (1 g cm^{-3}), χ_v is the dynamic shape factor in the free-molecular regime, $\chi_{v,inv}$ is the inverse of the free-molecular shape factor (= $1/\chi_v$), and S is the "Jayne shape

factor" as defined for the AMS by *Jayne et al.* [2000]. The last equality is effectively the definition of *S*. *S* is not the reciprocal of the dynamic shape factor χ_v. The relationship between χ_v and *S* can be derived using the relationship between D_m and D_v (equation 3) and will be presented in a future publication (P. DeCarlo et al., *in preparation*).

It is important to note that the vacuum aerodynamic diameter measured by the AMS is different from the classical aerodynamic diameter, which for a spherical particle equals the product of the physical diameter and the square root of the specific gravity [*Hinds,* 1999]. This diameter is measured when the expansion that imparts the size-dependent velocity to the particles occurs when the particles are in the continuum regime ($C_c \sim 1$). For example, the TSI Aerodynamic Particle Sizer operates near 1 atm and reports the sizes of particles above ~ 1 μm. Under these conditions, the classical aerodynamic diameter applies.

The effective particle density, ρ_{eff} is defined here as the product of the unit density by the ratio of the vacuum aerodynamic and mobility diameters. ρ_{eff} would be the material density of a spherical particle with the same vacuum aerodynamic and mobility equivalent diameters as the particles in our system. Combining Equations 6 and 9:

$$\rho_{eff} = \rho_0 \frac{D_{va}}{D_m} = \rho_p \frac{D_v}{\chi_v f(D_v, \chi, \lambda)} \tag{10}$$

Thus, the effective particle density reported here is equal to the material density for spherical particles. For non-spherical particles, the effective density is still proportional to the material density, but also depends on the particle shape through χ and χ_v. Additional information besides D_m and D_{va} would be needed to determine both the material density and the shape factors.

Figure 3.9 illustrates the variation of D_m, D_{va}, and ρ_{eff} with χ, under the assumptions of unit material density, D_v = 100 nm, and $\chi_v = \chi$. As the particle becomes more irregular (i.e., as χ increases), the mobility diameter increases and the vacuum aerodynamic diameter decreases. Thus, the effective density always decreases as χ increases.

The first estimate of particle effective density for our chamber experiments can be made from the observation reported above that the particle mass concentration measured by the AMS in the base case experiment (E1) starts to rise a few minutes earlier than the SEMS volume. This indicates that the AMS is detecting the mass of particles with a mobility diameter smaller than the SEMS detection limit of 25 nm (mobility). Since only particles larger than about 40 nm (vacuum aerodynamic) are efficiently transmitted by the AMS inlet, the effective density of the particles about 8 min after inception of photolysis can be estimated at about 2 g cm^{-3} or larger.

Using data for later times in the experiment for the dry base case (E1), the effective particle densities at 46 and 191 min since inception of photolysis are estimated from the SEMS particle volume mode and the AMS particle mass mode to be 1.22 and 0.86 g cm^{-3}, respectively. For the humid experiment (E2), particle effective densities after 46 and 191 min are estimated to be 2.2 and 1.6 g cm^{-3}, respectively. There is a tendency for decreasing effective density as the experiment progresses under both dry and humid conditions.

These effective densities are much lower than the material densities of the iodine oxides and oxyacids thought to comprise the aerosol (see below), all of which are larger than 4 g cm^{-3}. The low effective densities estimated for the particles formed in our chamber are consistent with particles being ramified structures of a solid material, most

likely fractal agglomerates. The decrease in effective density with time in the experiment suggests that the particles are becoming less compact as the experiment progresses, since the AMS indicates that the particle composition is not changing. The higher particle effective density observed under the humid experiment suggests that the structure has been made more compact by the water present in the system. This conclusion is consistent with the HTDMA results and with the decrease in the total apparent volume calculated from the SEMS data for the humid experiment as compared to the dry experiment.

3.5.2. Estimation of Particle Fractal Dimension

Both the HTDMA results and the particle effective density estimates suggest that the particles produced during chamber experiments-- especially those form under dry conditions-- are not dense compact structures and that they may be becoming less dense as the experiment progresses. It appears that coagulation produces agglomerates of smaller particles. The SEMS and AMS measurements reveal that the aerosol volume and mass concentrations and accompanying growth by condensation stop increasing after about 100 to 150 min of photooxidation for experiment E1. After this time, coagulation is expected to dominate particle growth, increasing the particle size and decreasing the number concentration. Particle losses to the chamber walls also contribute to the decreasing number concentration, and are estimated to become the dominant loss mechanism by 7 hours after the onset of photolysis. Hence, the time between 2.5 and 5 hours after the start of photolysis will be probed to examine the role of coagulation and agglomerate formation.

Growth of solid particles by coagulation often leads to structures that exhibit similarities over a wide range of scales. The masses of these so-called fractal structures scale with their radius as

$$m \approx m_1 \kappa \left(\frac{r}{r_1} \right)^{D_f} \tag{11}$$

where m_1 and r_1 are the mass and radius of the primary particles, and κ is an empirically derived geometry constant of order unity [*Wu and Friedlander,* 1993; *Sorensen and Roberts,* 1997]. Thus the collision radius, r, is

$$r \approx r_1 \left(\frac{m}{\kappa m_1} \right)^{\frac{1}{D_f}} \tag{12}$$

Small values of D_f indicate open, ramified structures with large apparent volumes, e.g., a linear chain of primary particles has a $D_f = 1$, while $D_f = 3$ corresponds to a solid sphere. Growth of agglomerate aerosols by Brownian coagulation with unit sticking probability results in values of $D_f \approx 1.75\text{-}1.8$ [*Friedlander,* 2000; *Sorensen,* 2001]. This process is called diffusion-limited aggregation (DLA). Reaction limited aggregation (RLA), for Brownian coagulation with low sticking probability yields values of 2.1-2.2. Higher fractal dimensions likely indicate that other processes are influencing the particle structure, e.g., coalescence.

We employ two techniques to estimate D_f from the experimental chamber data. The first method is based on the self-similar nature of the aerosol size distribution during coagulation. Under a wide range of collision frequency functions, coagulation leads to a particle size distribution that approaches an asymptotic form known as the self-preserving particle size distribution function [*Friedlander and Wang,* 1966]. This distribution is

expressed as $\psi(\eta) = Vn(v,t)/N^2$, in which $\eta = Nv/V$, where η is the dimensionless particle volume, ψ is the dimensionless particle size distribution function, v is the particle volume (cm^3), V is the particle volume concentration (cm^3 cm^{-3}), N is the particle number concentration (cm^{-3}) and $n(v, t)$ is the particle number density function at time t (μm^{-3} cm^{-3}). The existence of the self-preserving particle size distribution can be tested by plotting the dimensionless particle size distribution, e.g.,

$$\frac{d(N/N_{tot})}{d(D_p/\overline{D_p})} \tag{13}$$

versus the dimensionless particle size, $D_p/\overline{D_p}$, where $\overline{D_p}$ is the particle diameter with the same volume as the average volume of the size distribution. When size distributions measured at different times in the evolution of the aerosol collapse onto a single curve, that distribution is the self-preserving distribution. The shape of the self-preserving distribution depends on the transport regime, e.g., free molecular or continuum regime, and on the fractal dimension of the particles. Assuming Brownian coagulation and a constant fractal dimension during the entire growth process, *Vemury and Pratsinis* [1995] calculated the self-preserving distributions in the free-molecular and continuum regimes for agglomerates of various mass fractal dimensions. Since the free-molecular regime is applicable to particles below about 13 nm while the continuum regime concerns particles larger than about 1.3 μm, the chamber particles at the times of interest in this analysis are in the transition regime between the free-molecular and continuum regimes.

Figure 3.10 compares dimensionless SEMS measurements under dry conditions (Exp. E1) and self-preserving size distributions as computed by *Vemury and Pratsinis* [1995]. When coagulation is dominant, the measured size distributions closely approximate the

self-preserving distribution of agglomerates in the free molecular regime with a fractal dimension of about 2.5. Deviations from the continuum regime distribution (not shown) are large. After about 5 hours, D_f appears to decrease to about 2.3, probably reflecting the development of a more open agglomerate structure as particles grow by coagulation, and consistent with the above observation of reduced effective density as the experiment progresses.

The size distributions observed under humid conditions (Exp. E2, not shown) do not correspond to the self-preserving forms under either the free-molecular or continuum regimes. The difference must be due to a process other than coagulation. Wall losses are unlikely to differ significantly between dry and humid conditions. We speculate that water vapor induces structural rearrangement on a time scale comparable to that of coagulation, changing the coagulation kinetics and affecting the particle size distribution.

The second technique employed here allows estimation of the particle fractal dimension by examining the decay in the number concentration. *Flagan and Lunden* [1995] present an expression for the evolution of the average particle volume for an aerosol of fractal agglomerates at constant temperature in the free-molecular regime, which can be expressed as the relative number concentration decay under those conditions as

$$\frac{N(t)}{N_0} = \left[1 + 2^{2-\nu} \frac{6}{5} \left(\frac{3}{2} - \frac{\nu}{D_f} \right) \frac{t}{\tau_{coag}} \right]^{\frac{1}{\frac{\nu}{D_f} - \frac{3}{2}}} \tag{14}$$

where $N(t)$ is the number concentration at time t, N_0 is the initial number concentration, $\nu = \min(D_f, 2)$, and τ_{coag} is the characteristic time for coagulation. Thus, a plot of log N/N_0 versus log t reveals the characteristic time for coagulation from the break in the curve and

the fractal dimension from the slope at long times. For times small compared to τ_{coag}, the number concentration is close to N_0. At much longer times, the number concentration decays as $t^{\frac{1}{\nu}\frac{3}{D_f}-\frac{3}{2}}$, so the slope in the log-log plot at long times reveals the fractal dimension. This estimate is only approximate, however, because the aerosol undergoes a transition to less dense particles as coagulation begins to dominate. Figure 3.11 shows the decay in the theoretical and measured number concentrations starting at t_0 = 150 min after inception of photolysis. The number concentration is predicted to drop more rapidly for particles with smaller D_f, reflecting the larger coagulation rate of the looser agglomerates due to the increase in their collision area [*Matsoukas and Friedlander*, 1991; *Flagan and Lunden*, 1995]. From Figure 3.11, D_f is estimated at 1.9 decreasing to 1.8 for the dry experiment (E1) and 2.8 decreasing to 2.5 for the humid experiment (E2). This result reinforces the conclusions from the HTDMA measurements, the particle effective density estimates, and the self-preserving size distribution technique that (a) the particles produced in the humid experiment are more compact than those from the dry experiment; and (b) the particles tend to become less compact (decreasing D_f) as the experiment progresses. The values of D_f determined for the dry experiment are lower than the values (2.5 to 2.3) obtained from the self-preserving size distributions. This discrepancy may arise because of particle loss to the walls, which may make decay rates steeper than with coagulation only, leading to underestimation of D_f.

In summary, D_f for the dry experiment is estimated to be between 1.8-2.5. This is higher than the values of 1.75-1.8 for DLA, and of the same order than the values of 2.1-2.2 observed for RLA. This indicates that the particles in the dry experiment may not be undergoing significant restructuring after coagulation. The values of 2.8 to 2.5

determined for the humid experiment are larger than the values for either RLA or DLA. This indicates a modification of the primary particles after aggregation, consistent with our previous conclusion from the lack of agreement of the measured size-distribution with the self-preserving size distributions for fractal coagulation.

3.6 Gas-Phase Chemistry and Aerosol Uptake Kinetic Simulations

3.6.1. Gas Phase Mechanism

A zero-dimensional photochemical box model of the photolysis of CH_2I_2 in the presence of ozone is used in order to guide the interpretation of the observations. The chemical mechanism and reaction rate constants were adapted from *Sander* [1986]; *Vogt et al.* [1999]; *Cox et al.* [1999]; *McFiggans et al.* [2000]; *Atkinson et al.* [2000]; Ashworth *et al.* [2002]; and *Bloss et al.* [2001] and are given in Table 3.2. Photolysis rates have been modified, taking into account the difference between the UV and visible light intensities and spectral distributions in the chamber and at the Earth's surface.

Figure 3.12 shows a schematic of the gas-phase and aerosol uptake mechanism. Many of the gas-phase reactions in this diagram have been subjected to detailed laboratory studies and their rates and products are relatively well characterized. However, our knowledge of this chemistry is likely to be incomplete, and additional reactions not included in the mechanism may play a role in our chamber experiments [*Sander*, 2002; *McFiggans*, 2001; *Burkholder*, 2001]. Of the reactions in Figure 3.12, the largest uncertainties are in the aerosol uptake coefficients of iodine oxides and the role of I_2O_2 and I_2O.

OIO is active in the visible region of the spectrum and its cross section is relatively well characterized. A few groups have reported OIO cross sections, some of which are

only at a specific wavelength. *Bloss et al.* [2001] reported OIO cross section measurements in 514-573 nm. *Cox et al.* [1999] reported a value of $\sigma_{549nm} = 1.09 \cdot 10^{-17}$ cm^2, which agrees very well with the measurements of *Bloss et al* [2001]. *Ingham et al.* [2000] reported value of $\sigma_{549nm} = 3.5 \pm 1.5 \cdot 10^{-17}$ cm^2, which is a factor of three larger than either of the other three reports. In our simulations, we have used the cross section data reported by *Bloss et al.* [2001]. Two channels for OIO photolysis have been proposed:

$$OIO + h\nu \rightarrow IO + O(^3P) \qquad (i)$$

$$OIO + h\nu \rightarrow I + O_2 \qquad (ii)$$

The photodissociation threshold for OIO via channel (i) has been calculated to be ~415 nm [*Ashworth et al.*, 2002]; however, there are no measurements of OIO absorption spectrum in wavelengths shorter than 514 nm. Recent laboratory work indicates that the photolysis of OIO will lead to I atom formation [*Ashworth et al.*, 2002]. Thus, a unity quantum yield and a unity branching ratio have been assumed in the simulations for channel (ii). Based on detection of I in their experiments at low laser fluences, *Ingham et al.* (2000) placed a limit on the quantum yield of channel (ii) at 532 nm as <0.15. The structural sensitivity of the model to the channel of OIO photolysis has been evaluated with model runs, with 15% quantum yield of channel (ii).

The role of I_2O_2 also introduces significant uncertainties in the mechanism. I_2O_2 is a thermodynamically viable product of the IO self-reaction, according to the computational chemistry calculations of *Misra and Marshall* [1998], and has been tentatively identified in the gas phase [*Bloss et al.*, 2001]. Its photolysis rate has been assumed to be $1/5^{th}$ of the photolysis rate of IO [*McFiggans,* 2001]. However, it is likely that I_2O_2 thermally

decomposes rapidly based on extrapolating the decreasing thermal stability of the homologous compounds Cl_2O_2 and Br_2O_2 [*Sander*, 2002; *Burkholder*, 2001], which would contradict the results of Misra and Marshall. Given the significant uncertainties in those computational chemistry results, due to the limitations of the available basis sets for iodine at the time [*Sander*, 2002], we have assumed for our base case simulations a fast I_2O_2 thermal decomposition with τ_d = 50 ms. A series of sensitivity cases have also been run where the thermal decomposition has been turned off.

Another source of uncertainty is the fate of the $CH_2I\cdot$ radical after photolysis. *Cotter et al.* [2001] concluded that for their experimental investigation, conducted in the absence of O_3 and H_2O, the main path for $CH_2I\cdot$ was:

$$CH_2I\cdot + O_2 \rightarrow CH_2IOO\cdot$$

$$CH_2IOO\cdot + CH_2IOO\cdot \rightarrow CH_2IO\cdot + CH_2IO\cdot + O_2$$

$$CH_2IO\cdot \rightarrow CH_2O + I$$

In the chamber, reactions with other species may compete with self-reaction of the peroxy radical. In our mechanism, we have assumed that I is eventually released into the gas phase in a time scale that is short compared to that of CH_2I_2 photolysis. The formaldehyde produced will either photolyze or react with OH to yield CO, H_2, HO_2, and H_2O as final products [*Seinfeld and Pandis,* 1998]. A small fraction may partition onto the aerosol [*Jacob,* 2000].

Finally, it is possible that the gas-phase I_2 formed participates in the aerosol growth. I_2 is a solid with high vapor pressure (~ 0.2 Torr) at 20°C. The mechanism predicts that most of the I atoms will form I_2 when CH_2I_2 is photolyzed in the absence of O_3. However, no particles were formed in the experiments under these conditions, from

which we conclude that I_2 is not responsible for nucleation in this system. It is possible in principle that I_2 does condense on the particles after nucleation, and we have included this possibility as a mechanism variation study.

3.6.2. Aerosol Uptake Modeling

For the purposes of calculating uptake of gas-phase species, the aerosol is represented in a semi-empirical manner. Rather than trying to model particle nucleation and growth from first principles, we use the experimentally determined time-dependent size distribution as a basis for the calculations. Uptake of gas phase species (OIO, I_2O_2, HI, HOI, OH, and HO_2) onto the aerosol is calculated with the transition regime mass transfer formulation of Dahneke [*Seinfeld and Pandis,* 1998],

$$J = J_c \frac{1 + Kn}{1 + 2Kn(1 + Kn)/\alpha} \tag{15}$$

where J is the molecular flux (molec. s^{-1}) of the condensing species for a given particle, α is the uptake coefficient of the species on the particle, Kn is the Knudsen number of the particle, defined in this formulation as

$$Kn = \frac{2D_g}{\overline{c_A}} \tag{16}$$

where D_g is the diffusion coefficient of the condensable species in air, $\overline{c_A}$ is its average molecular velocity, and J_c is the molecular flux in the continuum regime,

$$J_c = 4\pi R_p D_g (c_\infty - c_s) \tag{17}$$

where R_p is the particle radius, and c_∞ and c_s are the concentrations of the species in the bulk gas and at the particle surface, respectively. For the simulations in this paper, c_s is assumed to be zero, and D_g is estimated for each species based on the diffusivity of

molecules of similar size and molecular weight in air. Then, equation (6) is integrated over the time-varying measured particle size distribution for each experiment.

No modification is needed to account for the influence of the fractal nature of the particles of the uptake of gas-phase species. *Rogak et al.* [1991] showed that spheres and agglomerates with the same mobility diameter have the same uptake rates of 1.5 nm lead clusters, which they used as a surrogate for a gas-phase species. Since the SEMS measures the mobility-equivalent diameter of the fractal particles, the uptake on the present particles will be the same as on spherical particles with the same mobility distribution. Thus, equations (6) and (8) can be applied directly to the experimentally determined mobility distribution.

The key parameter for the gas-to-particle mass transfer is the uptake coefficient α of each species. *McFiggans et al.* [2000] estimated uptake coefficients of the order of 0.03 for HI, HOI, OIO, and I_2O_2 onto aqueous aerosol, by tuning those values in their model of iodine chemistry in the marine boundary layer to optimize the agreement of available measurements. Studies of aerosol uptake of HOI and HI on ice, sodium halide salts, or sulfuric acid indicate uptake coefficients larger than 0.01 [*Percival et al*., 1999; *Holmes et al.*, 2001; *Mossinger at al.*, 2001]. However, such low uptake coefficients are not consistent with the observed particle growth in the chamber immediately after nucleation. The molecular flow, J_k (molec. s^{-1}) that can be supplied to a dense spherical particle in the free-molecular regime is [*Seinfeld and Pandis,* 1998]:

$$J_k = \pi R_p^2 \overline{c_A} \alpha (c_\infty - c_s) \tag{18}$$

Applying equation (9) to the first 10 seconds of nucleation in the base case (E1 and S1), R_p = 1.5 nm, $\overline{c_A}$ = 200 m s^{-1}, α = 0.036, c_∞ = 0.18 ppb OIO (from the simulations), and

c_s= 0, we obtain a flux of 0.24 molec. s^{-1}. If we assume that the particles detected by the CPC 3025 at that time have a size of 3 nm and are composed of pure OIO with the density of I_2O_4 (4.2 g cm^{-3}), a flux of about 22 molec. s^{-1} is needed to explain the rate of the observed nucleation burst. In order for both estimates to produce uptake rates of the same order-of-magnitude, the uptake coefficient needs to be of the order of 1 for whichever species is responsible for the initial nucleation burst. Based on this constraint, we assume in our model that uptake coefficients for OIO and I_2O_2 are 1.0, i.e., that every collision of a gas-phase molecule of those species with a particle results in the incorporation of the molecule into the particle, while the uptake coefficients of HOI and HI are assumed to be 0.03. Since the AMS indicates that the composition of the particles does not change during the experiment or with particle size, we assume here that the uptake coefficients for all iodine species that partition into the aerosol do not change either.

3.6.3. Kinetic Simulations: Major Paths and Time Scale Analysis

The mechanism predicts that none of the iodine-containing species considered in the literature as susceptible to being taken up into the aerosol (OIO, I_2O_2, HI, and HOI) is formed when either O_3 or UV radiation is not present. This prediction is consistent with the lack of aerosol formation under these experimental conditions. The cases simulated and the main results are summarized in Tables 3.3 and 3.4. We have chosen a base case simulation (S1) with initial gas-phase CH_2I_2 and O_3 mixing ratios of 5 and 100 ppb, respectively, and 2% RH, corresponding to the base case chamber experiment (E1). The predicted concentrations of iodine-containing species for case S1 vs. time are shown in Figure 3.13.

We illustrate the importance and relative speed of the different chemical paths with a time scale analysis here. Only the photolysis reactions have a fixed time scale, while molecule-molecule reactions as well as uptake processes change in time as functions of the concentrations of the other reactant, and the particle size distribution, respectively. Here, we have calculated all the time scales of the base case simulation S1 for 2 min after start of the photolysis, as well as for the time in which 63% of the iodine atoms are predicted to be in the aerosol phase, written as τ at 2-min / τ at 25-min.

The simulations indicate that CH_2I_2 is photolyzed with $\tau \sim 1.5$ min, releasing gaseous I radicals. The reaction of ozone with I to produce IO and the photolysis of IO to yield I are very fast ($\tau \sim 0.4$ s / 0.5 s, and 2.0 s, respectively). Self-reaction of IO to form I, OIO, I_2O_2, and I_2 is also relatively fast ($\tau \sim$ 7-140 s / 16-300 s), while the reaction of IO with $O(^3P)$ to form I is very slow ($\tau \sim$ 4 hr / 9 hr). Since I and IO interconvert very quickly, a local steady state is established between their concentrations. I_2O_2 is assumed to thermally decompose to IO ($\tau = 0.05$ s) in the base case. I_2O_2 is also photolyzed back to I ($\tau \sim 10$ s) and taken up by the aerosol ($\tau \sim$ 30 min / 10 s). OIO is photolyzed ($\tau \sim 2$ min) or taken up by the aerosol ($\tau \sim$ 25 min/ 10 s), with the first path dominating the fate of OIO at the beginning of the experiment and the second path doing so later on. Reaction with OH is about three orders of magnitude slower than photolysis as a relative loss rate for OIO.

I_2O is formed from I + IO ($\tau \sim$ 4 s / 9 s) and destroyed by reaction with I ($\tau \sim$ 5 s / 10 s). The second reaction is the main production route for I_2, while the formation of the latter species from I + I ($\tau \sim$ 40 min / 80 min) and IO + IO ($\tau \sim$ 2 min/ 5 min) are slower. I_2 remains in the gas phase until it is photolyzed ($\tau \sim 4.6$ min), since its reactions with O_3,

or $O(^3P)$ to from HOI, IO, I, and OIO are at least two orders of magnitude slower in terms of I_2 destruction.

Photolysis of a small amount of O_3 ($\tau \sim 28$ h) initiates a series of reactions that result in the formation of OH and HO_2 radicals, which reach concentrations of the order of 3 x 10^5 and 6 x 10^5 molec. cm^{-3}, respectively, at the time of 95% gas-to-particle conversion. The main loss channel for both radicals is the formation of HOI from I_2 + OH ($\tau \sim 0.07$ s / 0.1 s with respect to OH) and IO + HO_2 ($\tau \sim 3$ s / 7 s with respect to HO_2). HOI is incorporated into the aerosol ($\tau \sim 12$ h / 5 min) or photolyzed back to I ($\tau \sim 2.6$ min), while destruction of HOI by reaction with OH is negligible ($\tau > 9$ yr / > 3 yr). Conversion of I to HI is extremely slow ($\tau > 9$ yr / > 2 yr) with respect to I, and thus, HI is a very minor species in this case. Any amount of HI that is formed will be taken up by the aerosol ($\tau \sim 70$ min / 4 min) since its destruction by reaction with OH is very slow ($\tau \sim$ 225 h / 78 h).

The gas-phase products predicted to reach high concentration are OIO (in the early part of the experiment) and I_2, due to the high production rates (for both) and slower loss mechanism (for I_2). Ozone remains in excess at all times, and about 8 molecules of O_3 are predicted to be consumed per initial CH_2I_2 molecule in the base case. More than 99% of the iodine atoms are predicted to be in the aerosol phase 108 minutes after the inception of CH_2I_2 photolysis. The final calculated aerosol composition (mole fraction) is dominated by OIO (99.3% mole fraction), with the rest being made up by I_2O_2 and HOI in similar amounts (~0.3%).

3.6.4. Kinetic Simulations: Parametric Studies

A series of alternative cases have also been simulated using the standard mechanism in order to evaluate the effects of relative humidity, CH_2I_2 and O_3 initial concentrations, and UV radiation intensity. The main results of these cases are summarized in Table 3.3. The effect of the initial CH_2I_2 concentration is studied in cases S3 to S6. The predicted time scale of gas-to-particle conversion increases, and the O_3 consumption decreases with decreasing CH_2I_2 concentration. The changes in the time scale are mainly due to the slower aerosol uptake because of the smaller aerosol surface available, i.e., if the simulations are re-run with the size distribution of the base case (simulations S18 to S20), gas-to-particle time scales similar to that of the base case are obtained independently of the initial CH_2I_2 concentration.

The changes in aerosol composition with CH_2I_2 mixing ratio for the dry cases (with chamber lights) are illustrated in Figure 3.14. OIO is predicted to be the dominant aerosol species at all the CH_2I_2 concentrations used in the chamber experiments. HO_x and HOI are predicted to take over only for 1 ppt precursor concentrations (case S7, see below). The amount of HOI relative to OIO increases as CH_2I_2 decreases because the formation of HOI is first order in IO, while OIO formation is second order. I_2O_2 is a minor species in all cases, and it decreases as CH_2I_2 is decreased because the gas-phase I_2O_2 is preferentially thermalized or photolyzed as the time scale for aerosol uptake increases. The fraction of HO_2 and OH in the aerosol increases with decreasing CH_2I_2, and is predicted to make up a significant fraction of the aerosol at the lowest initial CH_2I_2 mixing ratios, which is somewhat surprising. The uptake coefficients of about 5×10^{-3} used here for both species are similar or smaller than those determined in the literature

for salt and soot aerosols [*Cooper and Abbatt*, 1996; *Ivanov et al.*, 1996; *Saathoff et al.,* 2001]. However the uptake coefficients used may not be appropriate for very small aerosol concentrations when saturation effects can be important. HI is a minor species in all cases, but its relative importance increases for low CH_2I_2 for the same reason than for HOI.

The effect of relative humidity is investigated with cases S2 and S9-S12, which are identical to the dry cases (S1 and S3-S6) except that RH is 65% instead of 2%. The main difference between the results of the humid cases with respect to the dry cases is that the relative importance of HOI in the predicted final aerosol increases roughly linearly with the amount of water vapor present, and becomes similar to OIO at 50 ppt CH_2I_2 and dominant at 15 ppt CH_2I_2. This is due to the much higher concentrations of HO_2 that are predicted to exist in the gas phase under humid conditions. The amount of HO_x in the aerosol also increases significantly, while that of I_2O_2 changes very little. The predicted time scale of gas-to-particle conversion does not change significantly with humidity, while O_3 consumption is enhanced at low concentrations in the humid cases as compared to the dry ones.

Cases S7 and S8 have been designed to simulate ambient conditions in coastal areas, as well as the effect of solar vs. chamber radiation. Marine boundary layer conditions were estimated as 1 ppt for CH_2I_2 (about the maximum amount that has been directly measured) 30 ppb for ozone, 76% RH, with a typical marine aerosol size distribution [*Vogt et al.*, 1999; *Seinfeld and Pandis*, 1998]. The predicted gas-to-particle time scale is ~ 16 h with chamber lights and 25 h with solar lights. In these cases, HO_2 and OH dominate the aerosol phase, followed by HOI. OIO is one to two orders of magnitude

smaller than HOI in the aerosol (lower with solar lights due to faster photolysis). Running the simulation with the solar lights (S8) rather than chamber lights (S7) increases the time scale of gas to particle conversion and depletes almost all of O_3 with only 78% of iodine converted to the particle phase.

The effect of the light spectrum (solar vs. chamber blacklights) is further investigated in case S13. The aerosol composition does not change significantly with solar light, with OIO still making up more than 98% of the aerosol molecules. The main differences when solar light is used in the simulation are a reduced gas-to-particle time scale and a large increase in the O_3 consumption. These effects are the result of much faster photolysis of OIO and I_2 with solar as compared to chamber lights. The faster photolysis of I_2 speeds up the aerosol uptake of total iodine species by eliminating the role of I_2 as the gas-phase reservoir species. The more rapid cycling of I to IO to OIO and I_2, and back to I from OIO and I_2 photolysis causes most of the enhancement on the O_3 destruction.

The effect of initial ozone concentration is investigated in cases S14 and S15. The main difference from the base case (S1) is that the time scale of gas-to-particle conversion is inversely proportional to the initial O_3 concentration. The reason for this trend is that increased initial O_3 results in higher IO and OIO concentrations and faster aerosol uptake. The differences in the aerosol composition and O_3 consumption are minor, as long as O_3 is in excess at all times.

Finally, the effect of UV light intensity is addressed in cases S16 and S17, which have one quarter and twice the photolysis rates of the base case for all species. The time scale of aerosol uptake in case S10 increases by only 25%, which is inconsistent with an increase by a factor of 2.7 in the experiments. The O_3 consumption in case S16 is

predicted to be 25% less than the base case, which again is an underestimate of the experimental observation of a 40% decrease. Both differences suggest that the chemical mechanism is incomplete in its photolysis reactions, or possibly in the reactions of the photolysis products.

3.6.5 Comparison of Experiments and Simulations

We have compared several simulation results with experimental data in order to assess the degree to which the simulations reproduce the observed phenomena. First, the lack of a humidity effect on the experimental observations of particle nucleation and growth is consistent with the lack of an important humidity effect on the outcome of the gas-phase chemical mechanism. However, the simulations predict a large increase in the amount of HOI in the aerosol under humid conditions over dry conditions, which is inconsistent with the lack of increase of the HIO_x signals in the humid experiment.

Second, Figure 3.6 compares the time scales of gas-to-particle conversion obtained from the simulations as a function of initial CH_2I_2 concentration. These time constants have the same order of magnitude as the experimental ones and show the same trend with CH_2I_2. The mechanism yields faster conversion than observed experimentally by about a factor of 1.8 to 2.2, except for the case of 0.015 ppb of CH_2I_2 initial concentration where the simulation predicts a slower conversion by ~30%. The simulations predict that the gas-to-particle time scale is controlled almost solely by the aerosol uptake process. Thus, this discrepancy could indicate that either the aerosol uptake is imperfectly modeled, or that the aerosol uptake is not the bottleneck of the gas-to-particle conversion process in the experiments.

Figure 3.15 shows a comparison of simulated and measured O_3 evolution for the base case (E1 and S1). The total O_3 consumed in the chamber is only 1/2 of the predicted value. Neither the experimental or simulated O3 are fitted well with a single exponential decay, but both agree very well with a double exponential fit. The time scales of the fast and slow exponential are 3.2 and 21 minutes for the simulations and 5.4 and 69 min. for the experimental data. This supports the previous conclusion that the gas-phase mechanism has imperfections that make it proceed too fast as compared with the experiments. The amount of O_3 destruction accounted for the fast (slow) exponential is 16 (7) ppb for the experiments and 7 (34) ppb for the simulations. Thus, the mechanism underpredicts the destruction of O_3 in the first few minutes by a factor of 2 but overpredicts the O_3 consumed at later times by about a factor of 5.

O_3 is consumed mostly by the reaction with I, with a smaller amount being produced from the reaction of O_2 with the $O(^3P)$ generated from IO photolysis. Since I and IO are rapidly interconverting, it seems that the mechanism underestimated the production of I in the first few minutes, but greatly overestimates it at later times. The smaller experimental consumption of O_3 at longer times suggests that the predicted regeneration of I via OIO, I_2, I_2O_2, and HOI photolysis, and IO self-reaction may be too fast in the mechanism.

Finally, the mechanism also does not predict the effects of decreased UV light intensity observed in the experiments as described above.

3.6.6. Kinetic Simulations: Results of the Alternative Mechanism Studies

The simulation results show qualitative agreement with some areas of disagreement with the chamber experiments. Since the rates of a number of mechanism steps are quite

uncertain, and even the structure of the mechanism is likely to be incomplete, we consider here additional simulations to evaluate whether some simple mechanism modifications, that are plausible in light of the current scientific knowledge about iodine kinetics, can bring the simulations closer to the experiments. These results are detailed in Table 3.4 and summarized in Table 3.5.

(a) *Variations of the I_2O_2 thermolysis.* The fate of I_2O_2 is one of the most uncertain steps in the mechanism. Two alternative cases are studied. Case S21 uses the same thermolysis rate and other conditions for the base case (S1) with a different product channel (2 I + O_2, instead of 2 IO, as assumed in the base mechanism). The predicted aerosol composition is not affected by this modification. The time scale of gas-to-particle conversion increases due to the reduction in IO concentration, which would reduce the gap with the experiments. However the simulated O_3 consumption almost doubles due to the increased release of I atoms from this thermolysis formulation, which increases the already large disagreement with the experiments.

In case S22, the I_2O_2 thermolysis has been turned off with respect to case S1. With this change, the amount of I_2O_2 in the predicted aerosol increases by a factor of 75, up to about 30% of the final mole fraction. The time scale of gas-to-particle conversion does not change much, but again, the O_3 consumption increases due to the liberation of I from the increased importance of I_2O_2 photolysis.

(b) *Faster aerosol uptake of HOI and HI.* The aerosol uptake coefficients of 0.03 used here for HOI and HI are based on experimental measurement of this uptake on different surfaces than the iodine species making up the aerosol in these experiments. Thus, it is possible that these uptake coefficients are larger, due to the increased affinity of HOI and

HI for the iodine-containing aerosol species. Case S23 is the same as the base case S1, with the exception of unity uptake coefficients for HI and HOI. However, the results of this mechanism change are very minor.

(c) *Uptake of I_2 by the aerosol after nucleation.* Although we have ruled out nucleation of I_2 as a new particle formation mechanism in our experiments, it is possible that some I_2 partitions onto the aerosol after nucleation. To bound the importance of this route, a series of cases (S24-S28) have been run with the maximum possible I_2 uptake (α = 1), as a function of CH_2I_2 concentration. In these cases, I_2 becomes the major component of the final aerosol. The time-scale of gas-to-particle conversion decreases compared to the base case simulations since I_2 shifts from being a reservoir gas phase species (lost only by photolysis to I with $\tau \sim 5$ min) to being rapidly taken up by the aerosol. This increases the discrepancy with the experimental time scales. In contrast, O_3 consumption decreases to a value closer to the experimental one.

(d) *Smaller quantum yield for OIO photolysis.* As mentioned above, the work by *Ingham et al.* [2001] suggests that the quantum yield of OIO photolysis is at most 15%--in contrast with the results of *Ashworth et al.* [2002]. Since this photolysis channel is still somewhat controversial, we have tested the effect of the lower OIO photolysis rate on the mechanism in cases S29-S33. As OIO is photolyzed slower, its aerosol uptake proceeds at a higher rate and the destruction of O_3 from the I released from OIO photolysis is smaller. The latter agrees better with the experimental results. However, the time scale of gas-to-particle conversion decreases, which brings the simulations even farther from the experiments.

(e) *OIO dimerization.* It has been suggested that the aerosol nucleation may start as OIO dimerization [*Hoffmann et al*., 2001]. If this were to happen, the dimers may protect OIO from photolysis. An upper bound for the OIO dimerization rate is about 1/100 of the collision rate [*Sander*, 2002]. Cases S34-S38 incorporate that rate of OIO dimerization, followed by uptake of the OIO dimer with $\alpha = 1$. The effects of this mechanism change are small decreases in the gas-to-particle time scale and the ozone consumption.

(f) *Slow release of second I atom after CH_2I_2 photolysis.* Finally, it is also possible that the release of the second I atom after CH_2I_2 photolysis is slower than we have assumed in our base case. To test the effects of this possibility, we have simulated two cases with the mechanism described above. The likely rate-limiting step is:

$$CH_2IOO\cdot + CH_2IOO\cdot \rightarrow CH_2IO\cdot + CH_2IO\cdot + O_2$$

We have computed two cases (S39 and S40) assuming that this reaction proceeds at 1/10 and 1/1000 of the collision rate. These modifications do not affect the main results because the rate is fast enough not to act as a bottleneck in the release of I into the gas phase. As the rate constant is decreased, $CH_2IOO\cdot$ builds up in the gas phase, resulting in a similar total rate. These results indicate that it is unlikely that the delay in release of the second I atom can result in the slower gas-to-particle conversion observed experimentally.

(g) *Fast reaction of OIO + I*: Cases S41-42 are designed to study the possible reaction of OIO and I at the collision rate of 1×10^{-10} cm^3 $molec^{-1}$ s^{-1} to form an isomer of I_2O_2 or $I_2 + O_2$, respectively. Neither of these two cases affect the aerosol composition much, while both cases increase the time scale of gas-to-particle conversion by ~40%-80%. S45 does not affect O_3 consumption, but S46 shows higher O_3 consumption

compared to the base case, which increases the disagreement with experimental observation.

(h) *Fast reaction of OIO + OH → HIO_3*: The possible observation of HIO_3 in the aerosol by the AMS is not explained by the known gas-phase chemistry. It is possible that OIO and OH could react to form HIO_3 rather than HOI [*McFiggans,* 2001], an oxyacid that if taken-up by the aerosols, might be the source of observed oxyacids in the experiments. Cases S43-S44 explore this possibility. A unity uptake coefficient has been assumed for HIO_3 to provide an upper bound of the contribution of this path. The results show no change in the time scale of gas-to-particle conversion or ozone consumption rate compared to the base case. The amount of HIO_3 formed in case S43 is one to two orders of magnitude too small to explain the signals of the HIO_2^+ and HIO_3^+ ions in the mass spectrometer. Additionally, the mechanism predicts a twenty-fold increase of the amount of HIO_3 in the aerosol when comparing the humid case (S44) to the dry case (S43), which is not consistent with the small decrease observed in the experiments. Thus, we conclude that this gas-phase path cannot explain the presence of iodine oxyacids in the particles.

The effect of all the mechanism variations is summarized in Table 3.5. No individual variation is able to bring the simulation results in line with the experimental data, indicating that our current understanding of gas-phase iodine chemistry is probably incomplete in several important ways.

3.7 Integrated Interpretation of the Aerosol Chemistry

This section pulls together all the available evidence to address two issues: the identity of the nucleating species and the chemical composition of the aerosol at later times. The AMS data reveal that the aerosol chemical composition does not vary with

time or particle size during the experiment, for particles large enough to be measured by the AMS (D_{va} > 40 nm, D_v > ~20 nm). This suggests that the nucleating species also comprise most of the aerosol at later times.

The gas-phase and aerosol uptake simulations predict an aerosol composed mostly of OIO and HOI, the latter becoming only important at lower CH_2I_2 concentrations. The mechanism also predicts the presence of small amounts of I_2O_2, HI, and the products of HO_2 and OH uptake in the aerosol.

The identity of the possible nucleating species can be probed by combining the results of the experiments and the gas-phase simulations. The predicted gas-phase concentrations at the time at which nucleation was observed experimentally are shown in Figure 3.16 as a function of initial CH_2I_2 mixing ratio. The orders of magnitude of the predicted gas-phase concentrations of the major species at the time of nucleation are 10^8-10^{11} molec. cm^{-3}. To put these levels in an atmospheric context, these concentrations are qualitatively similar to those of another atmospherically important system: H_2SO_4 / H_2O nucleate at ambient temperature at levels in the range 10^9-10^{11} molec. cm^{-3} [*Viisanen et al.*, 1997; *Ball et al.*, 1999], while H_2SO_4-NH_3-H_2O are estimated to nucleate when both H_2SO_4 and NH_3 reach levels around 2 x 10^7 molec. cm^{-3} [*Kulmala et al.*, 2002]. Coming back to our results, if a single species is nucleating in the chamber, the nucleation rate will be a very steep function of its supersaturation [*Seinfeld and Pandis,* 1998], i.e., its mixing ratio since all experiments were conducted at the same pressure and temperature. This should result in a "threshold" behavior, such that when that species reaches a critical concentration, nucleation ensues, which should appear as a nearly horizontal line for that species in Figure 3.16 vs. CH_2I_2. However, the concentration of all major species changes

by at least two orders of magnitude as the initial CH_2I_2 mixing ratio changes. This result reinforces the conclusion that the current knowledge of the gas-phase mechanism is incomplete.

The AMS data are consistent with the presence of iodine oxides in the particles, as well as that of water and/or iodine oxyacids. Pure iodine is a crystalline solid with a vapor pressure of ~0.2 Torr at ambient temperature. However, the fact that no particles are formed in the chamber when CH_2I_2 is photolyzed in the absence of O_3, yielding I radicals, indicates that pure iodine solid particles do not likely explain the observed nucleation behavior. Detection of I^+ and I_2^+ by the AMS and of the equivalent negative ions by *Hoffmann et al.* [2001] must stem from the thermal decomposition and/or fragmentation in the AMS of iodine oxides and/or hydrogen-containing iodine species in the particles.

Knowledge about iodine oxides is still incomplete. The existence of a number of oxides proposed in the literature has not been confirmed, including I_2O_3, I_2O_7, I_6O_{13}, and $I_{10}O_{19}$, [*Chase,* 1996]. The iodine oxides known to produce a stable solid phase are I_2O_4, I_2O_5, I_2O_6, and I_4O_9, while I_2O_2 has been tentatively identified in the gas phase [*Chase,* 1996; *Bloss et al.*, 2001]. Iodine oxides have a strong tendency to form polymeric networks. I_2O_4 can be approximated as a one-dimensional solid with infinite -I-O-IO_2-O- chains linked by weaker interchain I-O bonds [*Fjellvag and Kjekshus*, 1994]. I_2O_5 is composed of IO_2-O-IO_2 units linked by weaker I-O inter-unit bonds [*Selte and Kjekshus*, 1970]. I_2O_6 is composed of molecular subunits of composition I_4O_{12} linked by I-O bridges [*Kraft and Jansen,* 1995]. Little is known about the structure of I_4O_9. The chain structure of I_2O_4 and the simpler molecular structure of I_2O_5 seem more amenable to

rapid formation via gas-phase collisions during nucleation than the more elaborate structure of I_2O_6. Three of the oxides are known to decompose upon heating [*Fjellvag and Kjekshus,* 1994; *Kraft and Jansen*, 1995; *Maier and Bothur*, 1997; *Chase*, 1996] as

$$I_4O_9 \ (\sim 120°C) \rightarrow I_2 + O_2 + I_2O_5$$

$$I_2O_4 \ (\sim 200°C) \rightarrow I_2O_5 + I_2$$

$$I_2O_5 \ (\sim 400°C) \rightarrow I_2 + O_2$$

During the detection process of the AMS the particles are vaporized at ~600°C, probably undergoing a complex thermal decomposition. Thus, the I_2^+ detected with the AMS is consistent with any of the iodine oxides and does not imply the presence of pure iodine in the particles.

After vaporization in the AMS, the molecules are ionized by electron impact, and either the molecular ion or one of its fragments is detected by the mass spectrometer. This can explain the detection of I^+, IO^+, IO_2^+, IO_3^+, IO_5^+, I_2O^+, and $I_2O_3^+$ as fragments resulting from electron impact ionization of the products of vaporization of one or several iodine oxides. All of the *m/z* peaks detected for the chamber aerosol also appeared when sampling an I_2O_5 standard that had been diluted in water, atomized, and diffusion-dried. These peaks would very likely appear for the other iodine oxides as well, none of which is available commercially. Thus, the AMS data are consistent with the presence of I_2O_4 in the particles as suggested by *Hoffmann et al.* [2001] or with that of any other iodine oxide.

The signals at OH^+ and H_2O^+ could, in principle, arise for particle-bound water or from the decomposition of hydrogen-containing iodine species on the AMS vaporizer. The OH^+ and H_2O^+ signals increased by a factor of five between the dry and the humid

experiments, whereas the signals at HI^+, HIO^+, HIO_2^+, and HIO_3^+ were about half as large for the humid experiment as for the dry experiment. This indicates that the signals at OH^+ and H_2O^+ are likely due to particle-bound water.

The signals detected at HI^+, HIO^+, HIO_2^+, and HIO_3^+ indicate that the particles may also include hydrogen-containing iodine species, likely iodine oxyacids. Iodine acids reported in the literature include HI, HIO, HIO_2, HIO_3, and HIO_4. Gas-phase chemical mechanisms consider only HOI and HI, while the ionic species IO_3^- detected in aerosol samples is assumed to be formed by aqueous aerosol chemistry after uptake of other iodine species [*McFiggans et al.*, 2000; *Vogt et al.*, 1999]. The detection of HI^+ and HIO^+ could be due to HI and HOI present as such in the particles; however, their predicted aerosol concentrations are too low to explain the signal intensities detected in the AMS. The AMS detection of HIO_2^+ and HIO_3^+ indicates that either larger oxyacids are present in the particles (probably HIO_3), or that these are made on the AMS vaporizer from an iodine oxide and the particle-bound water. Both possibilities are plausible, although the former is more likely. Similar AMS signals were observed at HI^+, HIO^+, HIO_2^+, and HIO_3^+ when sampling I_2O_5 that had been dissolved in water-- a process that is known to produce HIO_3 [*Chase,* 1996]. The fact that *Hoffmann et al.* [2001] did not detect any hydrogen-containing ions is not necessarily inconsistent with the presence of HIO_3 in the particles, since the aerosol undergoes a much slower vaporization in their instrument at 550°C, during which HIO_3 can decompose by [*Chase,* 1996]:

$$HIO_3\ (\sim 200°C) \rightarrow I_2O_5 + H_2O$$

Little is known about the chemical decomposition that may occur when the particles impact the AMS vaporizer. It is possible that, if the particles are composed only of I_2O_4

and water, part of the I_2O_4 thermally decomposes on the AMS vaporizer to I_2O_5, which in turn, reacts with H_2O to yield the observed signals. However, the HIO_3 formed should further decompose at the higher temperatures of the AMS vaporizer.

If iodine oxyacids are present in the particles, their origin cannot be explained by the known gas-phase chemistry. *Sunder and Vikis* [1987] identified the solid product formed by the dark reaction of I_2 with O_3 under saturated water vapor conditions as HIO_3; however, this reaction had yielded only I_4O_9 when conducted under completely dry conditions [*Sunder et al.*, 1985]. The detailed gas-phase chemical mechanism is not known in either case, but is thought to involve the direct reaction of I_2 and O_3 to form a cyclic transition state that decomposes into either IO, I, and O_2, or IO_2 and IO, the latter path being non-negligible [*Vikis and MacFarlane,* 1985]. Since the water vapor concentration was very low in our dry experiments (RH < 2%), the chemistry leading to iodine oxyacids may have been different in our chamber than for the experiment of *Sunder and Vikis* [1987]. The presence of larger oxyacids in the particles could be a result of not yet known gas-phase chemistry or of the reaction of OH, HO_2, and/or H_2O with an iodine oxide in/on the particles. The reaction of OH and HO_2 with the particles cannot explain the observed intensity of HIO_x^+ signals, given the uptake coefficients that we have assumed, and that are similar to those determined in previous studies on salt aerosols, as described above. However, the much larger radical uptake coefficients that have been measured when a chemical reaction between the aerosol and the radical is involved [*Bertram et al.*, 2001] could result in the observed signals. Whichever is the actual formation path of iodine oxyacids under dry conditions, it is possible a non-

aqueous path is responsible for some of the IO_3^- detected in coastal aerosol samples, contrary to the prevailing literature assumption.

The HTDMA results provide another constraint on the aerosol composition. I_2O_5 and I_4O_9 are very hygroscopic (the former is known to yield HIO_3 in solution), while I_2O_4 is not. There is no information on the hygroscopicity of I_2O_6 or I_2O_2. The lack of hygroscopic growth of the aerosol formed in the humid experiment is inconsistent with an aerosol composed of either I_2O_5 or I_4O_9, while it is consistent with an aerosol composed mainly of I_2O_4.

Table 3.6 summarizes all of the available evidence about nucleating and condensing species. We conclude that homogeneous nucleation of OIO is the most likely mechanism for the observed nucleation bursts. The particles formed under dry conditions are composed of iodine oxides, likely I_2O_4, with some iodine oxyacids, likely HIO_3. A definitive chemical identification will necessitate the production of a larger mass of particles in a flow tube followed by an in-situ analysis technique, e.g., as described in *Sunder and Vikis* [1986].

3.8 Comparison to PARFORCE Results

While the mechanism studied in this paper is capable of producing very rapid and intense nucleation bursts, it is important to determine whether it is a good model for the mechanism that produced the observed nucleation bursts during the PARFORCE campaign described in the introduction [*O'Dowd et al.*, 2002], from whose results the mechanism tested in this paper was hypothesized. In this section, we evaluate this point by comparing the results of the chamber experiments presented in this paper with those of the PARFORCE campaign.

First, the chamber experiments indicate a lack of hygroscopic growth (growth factor ~ 1.0) in the HTDMA for particles formed under humid conditions. This is similar to the growth factors of 1.05 or less observed during nucleation events at Mace Head under low H_2SO_4 concentrations for 8-10 nm particles using a nano-HTDMA [*Väkevä et al.*, 2002, *O'Dowd et al.*, 2002]. These particles were found to contain either only iodine, or iodine and sulfate, while larger particles had a significantly larger sulfate to iodine ratio [*Mäkelä et al.*, 2002]. This suggests that the chemical composition of the newly formed particles may be the same in both cases. The low hygroscopicity points toward I_2O_4 as the major iodine oxide produced in both cases.

Second, we can also compare the nucleation and particle growth rates observed in the chamber with those observed during PARFORCE. During PARFORCE, the source rates of detectable sub-10 nm particles measured with a CPC array were 1-7 x 10^5 cm^{-3} s^{-1}. The particle growth rates were estimated at 0.1-0.36 nm s^{-1} from the CPC data and at 0.005-0.5 nm s^{-1} with a model based on the observations [*Hämeri et al.*, 2002; *O'Dowd et al.*, 2002]. Since O_3 and UV radiation will always be present at Mace Head during the daytime periods when nucleation was observed, we only need to determine the order of magnitude of CH_2I_2 (and other photolabile organic iodine species) during nucleation at PARFORCE to be able to compare field and chamber observations. The condensable vapor concentrations needed to explain the observed growth were estimated by two different models at 4-40 ppt and 240-440 ppt [*O'Dowd et al.,* 2002]. In measurements performed in coastal areas, mixing ratios of up to 6 ppt IO, 3 ppt OIO, and 0.45 ppt CH_2I_2 have been reported [*Alicke et al.,* 1999; *Allan et al.*, 2001; *Carpenter et al.*, 1999]. IO and OIO were detected with a long-path DOAS technique and may have been one to two

orders of magnitude higher over the shore areas [*O'Dowd et al.*, 2002], up to ~60-600 and ~30-300 ppt, respectively. Since CH_2I_2 photolyzes with a time scale of a few minutes and was measured with a slow instrument (1 hr), while the nucleation bursts at PARFORCE changed with a time scale of seconds, it is possible that the flux of iodine atoms from its photolysis at PARFORCE was significantly larger than the reported concentration of 0.45 ppt. From all the available data, we estimate that the amount of iodine present in gas-phase species that originate from CH_2I_2 is in the range 4-600 ppt. Thus, we will use the results of the chamber experiments with 15, 50 and 500 ppt CH_2I_2 (Exp. E3, E4 and E5) to provide order of magnitude estimates of the nucleation and growth rates. The source rates of sub-10 nm particles in the chamber during those experiments are 10^3-10^6 cm^{-3} s^{-1}, while the growth rates of the nucleated particles are 0.005-0.08 nm s^{-1}. Thus; the source and growth rates observed in the chamber are reasonably consistent with those observed in the field experiments, given the large uncertainties present in both sets of ultrafine particle measurements, and on the estimated precursor concentration at PARFORCE.

Kulmala et al. [2002] propose that the nucleation and particle growth steps could have been decoupled during PARFORCE, with H_2SO_4-NH_3-H_2O providing the nuclei for another species to condense on. Our laboratory results indicate that photooxidation of CH_2I_2 can result in nucleation and particle growth rates similar to those observed in coastal areas, and thus, that ternary nucleation of H_2SO_4-NH_3-H_2O need not be invoked.

Finally, the results in this paper provide an explanation of the lack of correlation between O_3 and particle formation during PARFORCE, with the exception of one strong nucleation event in which O_3 was noticeably reduced [*O'Dowd et al.*, 2002]. The total O_3

consumption predicted by the chemical mechanism for the chamber experiments between 15 and 500 ppt CH_2I_2 is ~2-7 ppb over a time scale of 20 min. These estimates can be used as an upper bound of O_3 destruction since the simulations overpredict the measured O_3 destruction for the 5 ppb experiments by a factor of 2 (Figure 3.15). From these results, we estimate an O_3 destruction rate of at most 0.1-0.35 ppb min^{-1}, which would be difficult to detect on top of fluctuations on a natural background of the order of 30 ppb and the noise of the O_3 analyzer itself. Also, since this chemical system consumes little O_3 and is insensitive to the O_3 concentration (as long as there is excess O_3), it is unlikely that ozone will ever be the limiting reactant. If CH_2I_2 (or other photolabile organic iodine species) is available at concentrations of tens of ppt together with UV light, new particle formation will proceed.

3.9. Conclusions

We have studied the photooxidation of CH_2I_2 in the presence of O_3 experimentally in the Caltech indoor chamber and by means of gas-phase chemical simulations. We can summarize the observed aerosol dynamics in the base case experiment (Exp. E1, 5 ppb CH_2I_2, 100 ppb O_3, RH < 2%) as: (1) a nucleation burst immediately after the inception of photolysis with its highest intensity for about 1 min; (2) condensation of additional vapors onto the nucleated particles for a period of 1.5-2.5 h; (3) particle coagulation, which occurs after the nucleation burst and controls the dynamics from the point when condensation ceases; and 4) a size-dependent wall loss of particles, which is important for the freshly nucleated particles and later has a characteristic time of about 5 h. Particles formed under dry conditions are fractal agglomerates with mass fractal dimensions, D_f ~ 1.8-2.5. Higher relative humidity does not alter the nucleation or growth behavior, but

results in more compact and dense particles (D_f ~ 2.5-2.8). The main features of this process do not change with decreasing initial CH_2I_2 concentration; however, the gas-to-particle conversion is slower, likely due to reduced aerosol surface for uptake.

Based on all the available information, the most likely species that could be responsible for the observed nucleation bursts and condensation growth is OIO. Chemical analysis of the particles is consistent with the presence of iodine oxides, although the available evidence is inconclusive for any one of them. Water and/or iodine oxyacids-- likely HIO_3-- are also present in the particles. The acid may be formed in the gas phase or by reactions in/on the aerosol. Comparison between particle hygroscopicity, composition, and nucleation and growth rates observed in coastal measurements and in the present experiments suggest that photooxidation of CH_2I_2-- possibly coupled with other photolabile organic iodine species-- is the mechanism leading to the observed new particle formation on the west coast of Ireland. For CH_2I_2 concentrations of tens of ppt during daylight hours, new particle formation can occur without the need for pre-existing clusters from species outside the iodine system.

3.10. Acknowledgements

This work was supported by U. S. Department of Energy grant DE-FG03-01ER63099. The authors sincerely thank Stan Sander, Kyle Bayes, and Daniel Milligan of the NASA Jet Propulsion Laboratory, Gordon McFiggans of UMIST, Mitchio Okumura and Paul Wennberg of Caltech, Jim Burkholder and Joachim Curtius of the NOAA Aeronomy Laboratory, and Xiao-Ying Yu of Colorado State University for useful suggestions about iodine kinetics.

3.11. References

Aitken, J.A. On some nuclei of cloudy condensation Part I. *Trans. Roy. Soc. Edin.,* XXXIX, 1897; *Nature* LVI.

Alicke, B.K., K. Hebestreit, J. Stutz, and U. Platt. Iodine oxide in the marine boundary layer. *Nature, 397*, 572-573, 1999.

Allan, B.J., J.M.C. Plane, and G. McFiggans. Observations of OIO in the remote marine boundary layer. *Geophys. Res. Letters, 28*, 1945-1948, 2001.

Ashworth, S.H., B.J. Allan, and J.M.C. Plane. High resolution spectroscopy of the OIO: implications for the ozone-depleting potential of iodine in the marine boundary layer. *Submitted to Geophysical Research Letters,* 2002.

Atkinson, R., D.L. Baulch, R.A. Cox, R.F. Hampson, J.A. Kerr, M.J. Rossi, and J. Troe, Evaluated kinetic and photochemical data for atmospheric chemistry: Supplement VIII, halogen species, *J. Phys. Chem. Ref. Data, 29*, 167-266, 2000.

Ball, S.M., D.R. Hanson, F.L. Eisele, and P.H. McMurry. Laboratory Studies of Particle Nucleation: Initial Results for H_2SO_4, H_2O, and NH_3 vapors. *J. Geophys. Res., 104*, 23,709-23,718, 1999.

Baron, P.A., and Willeke, K. Gas and Particle Motion. In *Aerosol Measurement: Principles, Techniques, and Applications*; Baron, P.A., and Willeke, K., Eds.; John Wiley & Sons, New York, 2001.

Behrens, D., G. Kreysa, and R. Eskermann. Eds., *DECHEMA Corrosion Handbook: Corrosive Agents and Their Interaction with Materials, Volume 3, Acid Halides, Amine Salts, Bromides, Bromine, Carbonic Acid, Lithium Hydroxide*. John Wiley and Sons, New York, 1989.

Bertram, A.K., A. Ivanov, M. Hunter, L.T. Molina, and M. J. Molina. The Reaction Probability of OH on Organic Surfaces of Tropospheric Interest. *J. Phys. Chem. A,*105: 9415-9421, 2001.

Bloss, W.J., D.M. Rowley, R.A. Cox, and R.L. Jones. Kinetics and Products of the IO Self-Reaction. *J. Phys. Chem. A, 105*, 7840-7854, 2001.

Burkholder, J. Aeronomy Laboratory, National Oceanic and Atmospheric Administration, Boulder, Colorado. Personal Communication, 2001.

Carpenter, L.J., W.T. Sturges, S.A. Penkett, P.S. Liss, B. Alicke, K. Hebestreit, and U. Platt. Short-lived alkyl iodides and bromides at Mace Head, Ireland: links to biogenic sources and halogen oxide production. *J. Geophys. Res., 104*, 1679-1689, 1999.

Carter, W.P.L, D. Luo, I.L. Malkina, and J.A. Pierce. Environmental chamber studies of atmospheric reactivities of volatile organic compounds. Effects of varying chamber and light source. *Final report to National Renewable Energy Laboratory*, 1995. ftp://ftp.cert.ucr.edu/pub/carter/pubs/explrept.pdf

Chase, M.W. NIST-JANAF thermochemical tables for the iodine oxides. *J. Phys. Chem. Ref. Data, 25*, 1297-1340, 1996.

Cocker, D.R., R.C. Flagan, and J.H. Seinfeld. State-of-the-art chamber facility for studying atmospheric aerosol chemistry. *Env. Sci. Technol. 35*, 2,594-2,601, 2001.

Collins D. R., R.C. Flagan, and J.H. Seinfeld. Improved inversion of scanning DMA data. *Aerosol Sci. Technol.,* 36: 1-9, 2002.

Cooper, P.L. and J.P.D. Abbatt. Heterogeneous interactions of OH and HO_2 radicals with surfaces characteristics of atmospheric particulate matter. *J. Phys. Chem., 100,* 2249-2254, 1996.

Cotter, E.S.N., Booth, N.J., Canosa-Mas, C.E., and Wayne, R.P.. Release of Iodine in the Atmospheric Oxidation of Alkyl Iodides and the Fates of Iodinated Alkoxy Radicals. *Atmos. Environ.*, 35, 2169-2178, 2001.

Cox, R.A., W.J. Bloss, R.L. Jones, and D.M. Rowley. OIO and the atmospheric cycle of iodine. *Geophys. Res. Letters, 26*, 1,857-1,860, 1999.

De More W.B., S.P. Sander, D.M. Golden, R.F. Hampson, M.J. Kurylo, C.J. Howard, A.R. Ravishankara, C.E. Kolb and M.J. Molina. Chemical Kinetics and Photochemical Data for Use in Stratospheric Modeling. *Evaluation 12, JPL NASA*, 1997.

Finlayson-Pitts, B.J., and J.N. Pitts. *Chemistry of the upper and lower atmosphere: theory, experiments and applications.* Academic Press, San Diego, 2000.

Fjellvag, H., and A. Kjekshus. The crystal structure of I_2O_4 and its relations to other iodine-oxygen-containing compounds. *Acta Chemica Scandinavica, 48,* 815-822, 1994

Flagan, R.C. Electrical Techniques. In *Aerosol Measurement: Principles, Techniques, and Applications*. Baron, P.A., and Willeke, K., Eds.; John Wiley & Sons, New York, 2001.

Flagan, R. C., and M.M. Lunden. Particle structure control in nanoparticle synthesis from the vapor phase. *Materials Science and Engineering*, *A204*, 113-124, 1995.

Flagan, R.C., S.-C. Wang, F. Yin, J.H. Seinfeld, G. Reischi, W. Winklmayr, and R. Karch. Electrical mobility measurements of fine-particle formation during chamber studies of atmospheric photochemical reactions. *Environ. Sci. Technol., 25*, 883-890, 1991.

Friedlander, S. K. and C.S. Wang. The self-preserving Distribution for Coagulation by Brownian Motion. *J. Colloid Interface Sci*., *22*, 126, 1966.

Friedlander, S.K. *Smoke, Dust, and Haze: Fundamentals of Aerosol Dynamics, 2nd Ed.* Oxford University Press, New York, 2000.

Fuchs, N.A. *The Mechanics of Aerosols*. Pergamon Press, New York, 1964.

Grenfell, J.L., R.M. Harrison, A.G. Allen, J.P. Shi, S.A. Penkett, and C.D. O'Dowd. An analysis of rapid increases in condensation nuclei concentrations at a remote coastal site in western Ireland. *J. Geophys. Res., 104*, 13771-13780, 1999.

Hämeri, K., C.D. O'Dowd, and C. Hoell. Evaluating measurements of new particle concentrations, source rates, and spatial scales during coastal nucleation events using condensation particle counters. *J. Geophys. Res.*, *107(D19)*, 8101, doi:10.1029/2001JD000411, 2002.

Hinds, W.C. *Aerosol Technology*, John Wiley & Sons, New York, 1999.

Hoffmann, T., C.D. O'Dowd, and J.H. Seinfeld. Iodine oxides and new particle formation in the coastal boundary layer. *Geophys. Res. Letters, 28*, 1949-1952, 2001.

Holmes, N.S., J.W. Adams, and J.N. Crowley. Uptake and reaction of HOI and $IONO_2$ on frozen and dry NaCl/NaBr surfaces and H_2SO_4. *Phys. Chemistry Chem. Phys., 3*, 1679-1687, 2001

Ingham, T., M. Cameron, and J.N. Crowley. Photodissociation of IO (355 nm) and OIO (532 nm): Quantum Yields for $O(^3P)$ and $I(^2P_J)$ Production. *J. Phys. Chem., 104*, 8001-8010, 2000.

Ivanov, A.V., Y.M. Gershenzon, F. Gratpanche, P. Devolver, and J.-P. Sawerysyn. Heterogeneous loss of OH on NaCl and NH_4NO_3 at tropospheric temperatures. *Annales Geophysicae, 14*, 659-664, 1996.

Jacob, D.J. Heterogeneous chemistry and tropospheric ozone. *Atmos. Environ.,* 34, 2131-2159, 2000.

Jayne, J.T., D.C. Leard, X. Zhang, P. Davidovits, K.A. Smith, C.E. Kolb, and D.R. Worsnop. Development of an aerosol mass spectrometer for size and composition. analysis of submicron particles. *Aerosol Sci. Technol., 33*, 49-70, 2000.

Jimenez, J.L., J.T. Jayne, Q. Shi, C.E. Kolb, D.R. Worsnop, I. Yourshaw, J.H. Seinfeld, R.C. Flagan, X. Zhang, K.A. Smith, J. Morris, and P. Davidovits. Ambient Aerosol Sampling with an Aerosol Mass Spectrometer. *J. Geophys. Res*, in press, 2002.

Kraft, T., and M. Jansen. Synthesis and crystal structure of diiodine (V/VII) hexaoxide: An intermediate between a molecular and a polymer solid. *J. Am. Chem. Soc., 117,* 6,795-6,796, 1995.

Kulmala, M., A., P. Korhonen, I. Napari, A. Karlsson, H. Berresheim, and C.D. O'Dowd. Aerosol Formation during PARFORCE: Ternary Nucleation of H_2SO_4, NH_3, and H_2O. *J. Geophys. Res.,* 107, 10.1029/2001JD000900, 2002.

Laturnus, F. Volatile halocarbons released from artic macroalgae. *Mar. Chem., 55*, 359-366, 1996.

Maier, G. and A. Bothur. Matrix-isolation of iodine superoxide and iodine dioxide. *Chem. Ber./Recueil, 130,* 179-181, 1997

Mäkelä, J.M., T. Hoffmann, C. Holzke, M. Väkevä, T. Suni, T. Mattila, P.P. Aalto, U. Tapper, E. Kaupinen, and C. D. O'Dowd. Biogenic iodine emissions and identification of end-products in coastal ultrafine particles during nucleation bursts. *J. Geophys. Res.*, *107 (D19)*, 10.1029/2001JD000580, 2002.

Matsoukas, T. and Friedlander, S. K. *J. Colloid Interface Sci.*, *146*, 495, 1991.

McFiggans, G., J.C. Plane, B.J. Allan, L.J. Carpenter, H. Coe, and C.D. O'Dowd. Modeling Study of Iodine Chemistry in the Marine Boundary Layer. *J. Geophys. Res.*, *105*, 14,371-14,385, 2000.

McFiggans, G. Department of Physics, UMIST, Manchester, United Kingdom. Personal Communication, 2001.

McMurry, P.H., X. Wang, K. Park, and K. Ehara. The Relationship between Mass and Mobility for Atmospheric Particles: A New Technique for Measuring Particle Density. *Aerosol Sci. Technol.* 36: 227–238 (2002).

Milligan, D. Jet Propulsion Laboratory, Pasadena, California. Personal communication, 2002.

Misra, A., and P. Marshall. Computational investigations of iodine oxides. *J. Phys. Chem. A, 102*, 9056-9060, 1998

Mössinger, J.C., D.E. Shallcross, and R.A. Cox. UV absorption cross-sections and atmospheric photolysis rates of CH2Br2, CH2I2 and CH2BrI. *J. Chem. Soc., Faraday Trans., 94*, 1391-1396, 1998.

Mössinger, J.C., and Cox, R.A. Heterogeneous Reaction of HOI with Sodium Halide Salts. *J. Phys. Chem. A.,* 105: 5165-5177, 2001.

O'Dowd, C.D., M. Geever, M. K. Hill, M.H. Smith, and S.G. Jennings. New particle formation: Nucleation rates and spatial scales in the clean marine coastal environment. *Geophys. Res. Lett., 25,* 1661-1664, 1998.

O'Dowd, C.D., G. McFiggans, D. Creasey, L. Pirjola, C. Hoell, M.H. Smith, B.J. Allen, J.M.C. Plane, D.E. Heard, J.D. Lee, M.J. Pilling, and M. Kulmala. On the photochemical production of new particles in the coastal boundary layer. *Geophys. Res. Lett., 26*, 1707-1710, 1999.

O'Dowd, C.D., K. Hämeri, J. M. Mäkelä, L. Pirjola, M. Kulmala, S.G. Jennings, H. Berresheim, H-C. Hansson, G. de Leeuw, G.J. Kunz, A.G. Allen, C.N. Hewitt, A. Jackson, Y. Viisanen and T. Hoffmann. A dedicated study of new particle formation and fate in the coastal environment (PARFORCE): Overview of objectives and achievements. *J. Geophys. Res.*, *107*, 10.1029/2001JD000555, 2002.

Percival, C.J., Mössinger, J.C., and Cox, R.A.. The Uptake of HI and HBr on Ice. *Phys. Chem. Chem. Phys.,* 1, 4565-4570, 1999.

Rader D. J. and P.H. McMurry. Applications of the Tandem Differential Mobility Analyzer to Studies of Droplet Growth or Evaporation. *J. Aerosol Sci., 17*, 771-787, 1986.

Rogak, S.N., U. Balstensperger, and R.C. Flagan. Measurement of mass transfer to agglomerate aerosols. *Aerosol Sci. Technol.*, 14, 447-458, 1991.

Rowley, D., J.C. Mossinger, R.A. Cox, R.L. Jones. The UV-visible absorption cross-section and atmospheric photolysis rate of HOI. *J. Atmos. Chem., 34,* 137-151, 1999.

Saathoff, H., K.H. Naumann, N. Riemer, S. Kamm, O. Mohler, U. Schurath, H. Vogel, and B. Vogel. The loss of NO_2, HNO_3, NO_3/N_2O_5, and $HO_2/HOONO_2$ on soot aerosol: A chamber and modeling study. *Geophys. Res. Letters, 28,* 1957-1960, 2001.

Sander, S.P. Kinetics and mechanism of the IO+IO reaction. *J. Phys. Chem., 90,* 2194-2199, 1986.

Sander, R., R. Vogt, G.W. Harris, and P.J. Crutzen. Modeling the chemistry of ozone, halogen compounds, and hydrocarbons in the arctic troposphere during spring. *Tellus, 49B,* 522-532, 1997.

Sander, S.P. Jet Propulsion Laboratory, Pasadena, California. Personal communication, 2002.

Seinfeld, J.H., and S.N. Pandis. *Atmospheric chemistry and physics: from air pollution to climate change*. John Wiley, New York, 1998.

Selte, K., and A. Kjekshus. Iodine oxides. Part III. The crystal structure of I_2O_5. *Acta Chemica Scandinavica, 24,* 1912-1924, 1970.

Sorensen, C.M., and G.C. Roberts. The prefactor of fractal aggregates. *J. Colloid Interface Sci. 186*, 447–452 1997.

Sorensen, C.M. Light scattering by fractal aggregates: a review. *Aerosol Sci. Technol.*, 35, 648-687, 2001.

Sunder, S., J.C. Wren, and A.C. Vikis. Raman spectra of I_4O_9 formed by the reaction of iodine with ozone. *Journal of Raman Spectroscopy, 16*, 424-426, 1985.

Sunder, S., and A.C. Vikis. Raman spectra of iodine oxyacids produced by the gas-phase reaction of iodine with ozone in the presence of water vapour. *Canadian Journal of Spectroscopy, 32,* 45-48, 1987.

TSI, Model 3025A *Ultrafine Condensation Particle Counter Operation and Display Instruction Manual*. TSI, Inc., St. Paul, Minnesota, 1996.

Väkevä, M., K. Hämeri, and P. Aalto. Hygroscopic properties of nucleation mode and Aitken mode particles during and outside nucleation bursts in west coast of Ireland. *J. Geophys. Res.,107,* 10.1029/2000JD000176, 2002.

Vemury, S. and S.E. Pratsinis. Self-preserving size distributions of agglomerates. *J. Aerosol Sci.*, *26*, 175-185, 1995.

Viisanen, Y., M. Kulmala, and A. Laaksonen. Experiments on Gas-Liquid Nucleation of Sulfuric Acid and Water. *J. Chem. Phys., 107*, 920-926, 1997

Vikis, A.C., and R. MacFarlane. Reaction of iodine with ozone in the gas phase. *J. Phys Chem., 89,* 812-815, 1985.

Vogt, R., R. Sander, R. Von Glasow, and P.J. Crutzen. Iodine chemistry and its role in halogen activation and ozone loss in the marine boundary layer: a model study. *J. Atmos. Chem., 32,* 375-395, 1999.

Wang S.C. and R.C. Flagan. Scanning electrical mobility analyzer. *J. Aerosol Sci., 8*, 1485-1488, 1989.

Weber, R.J., P.H. McMurry, R.L. Mauldin III, D.J. Tanner, F.L. Eisele, A.D. Clarke, and V.N. Kapustin. New Particle Formation in the Remote Troposphere: A Comparison of Observations at Various Sites. *Geophys. Res. Letters, 26*, 307-310, 1999.

Weingartner, E., H. Burtscher, and U. Baltensperger. Hygroscopic properties of carbon and diesel soot particles. *Atmos. Environ.*, 31, 2311-2327, 1997.

Wu, M.K., and S.K. Friedlander. Note on the power law equation for fractal-like aerosol agglomerates. *J. Colloid Interface Sci.*, 159, 246-248, 1993.

Table 3.1. Summary of the experiments performed

Experiment	CH_2I_2 (ppb)	O_3 Initial (ppb)	Relative Humidity (%)	Radiation Intensity (Relative to Full Power)[a]	Delay from Photolysis to Nucleation (s)	Max. Number (cm^{-3})	Max. Area (μm^2 cm^{-3})	Max. Volume (μm^3 cm^{-3})	Mode Diameter at 2 h (nm)	Time scale of volume (min)[b]
E1 (Base case)	5	100	< 2	1	31	$1.7 \cdot 10^6$	2600	85	100	45
E2	5	100	65	1	36	$1.6 \cdot 10^6$	2300	50	85	50
E3	0.5	100	< 2	1	80	$3.5 \cdot 10^5$	640	14	65	110
E4	0.05	100	< 2	1	145	$9.0 \cdot 10^4$	300	4	38	220
E5	0.015	100	< 2	1	720	$4.0 \cdot 10^3$	70	1.2	30	470
E6	50	500	< 2	1	15	$8.2 \cdot 10^6$	22,000	1002	200	21[c]
E7	5	100	<2	0.25	44	$1.5 \cdot 10^6$	3,000	100	100	120
E8 [c]	5, 0.5, 0.05, and 0.015	100	<2 and 65	0	No particle formation observed					
E9	5	0	< 2	1	No particle formation observed[d]					

[a] Measured 2.9 W m^{-2} nm^{-1} at the peak of 354 nm, with the spectral dependence described by *Cocker et al.* [2001].
[b] Defined as the time at which the volume concentration reaches 1 - 1/e (~63%) of its maximum value.
[c] Estimated from the AMS mass signal since the SEMS is saturated for some particle sizes.
[d] *Hoffmann et al.* [2001] report that particle formation was "drastically reduced," but not completely eliminated, when O_3 was not added to the chamber. We observed no particle formation at all, until O_3 started to build up in the chamber, an unavoidable phenomenon due to a small rate of O_3 formation from trace amounts of VOCs and NO_x in the feed air. The presence of a small amount of O_3 from this source probably explains the detection of some particles by *Hoffmann et al.* [2001] when no external O_3 was added.

Table 3.2. Chemical mechanism used in the gas-phase and aerosol uptake simulations.

No.	Reaction	Rate Constant ‡	Rate at 20°C ‡	Notes
1.	$CH_2I_2+h\nu \rightarrow CH_2+2I$		1.12×10^{-2}	1
2.	$I+O_3 \rightarrow IO+O_2$	$(2.3 \times 10^{-11}) \times \exp(-870/T)$	1.18×10^{-12}	10
3.	$I+I+M \rightarrow I_2+M$	$[M]*1.7 \times 10^{-32}$	4.17×10^{-13}	3
4.	$O(^3P)+I_2 \rightarrow IO+I$	1.4×10^{-10}	1.4×10^{-10}	10
5.	$IO+IO \rightarrow OIO+I$ (38%) $\rightarrow I_2O_2$ (48.5%) $\rightarrow 2I+O_2$ (11%) $\rightarrow I_2+O_2$ (2.5%)	$(4.1 \times 10^{-11}) \times \exp(220/T)$	8.68×10^{-11}	12
6.	$I+HO_2 \rightarrow HI+O_2$	$(1.5 \times 10^{-11}) \times \exp(-1090/T)$	3.6×10^{-13}	10
7.	$IO+HO_2 \rightarrow HOI+O_2$	$(9.0 \times 10^{-12}) \times \exp(680/T)$	9.2×10^{-11}	5
8.	$O(^3P)+IO \rightarrow O_2+I$	1.4×10^{-10}		5
9.	$OH+HI \rightarrow I+H_2O$	$(1.6 \times 10^{-11}) \times \exp(440/T)$	7.2×10^{-11}	5
10.	$HOI+OH \rightarrow IO+H_2O$	2×10^{-13}	2×10^{-13}	2
11.	$OH+I_2 \rightarrow HOI+I$	2.1×10^{-10}	2.1×10^{-10}	5
12.	$OH+OIO \rightarrow HOI+O_2$		2.0×10^{-10}	13a
13.	$I+IO+M \rightarrow I_2O+M$	1.7×10^{-10} (at 22°C)		12
14.	$I+I_2O \rightarrow I_2+IO$	2.1×10^{-10} (at 22°C)		12
15.	$I_2+O_3 \rightarrow IO+I+O_2$ (50%) $\rightarrow IO+OIO$ (50%)		3.68×10^{-18}	14
16.	$I_2+h\nu \rightarrow 2I$		0.0036	6
17.	$IO+h\nu \rightarrow I+O(^3P)$		0.50	7
18.	$OIO+h\nu \rightarrow$ $\rightarrow I+O_2$		0.0084	11 12
19.	$HOI+h\nu \rightarrow I+OH$		0.0063	8
20.	$I_2O_2+h\nu \rightarrow 2I+O_2$		0.1	13b
21.	$I_2O_2+M \rightarrow 2IO$		20	15
22.	$O(^1D)+N_2 \rightarrow O(^3P)+N_2$	$(1.8 \times 10^{-11}) \times \exp(110/T)$	2.6×10^{-11}	10
23.	$O(^1D)+O_2 \rightarrow O(^3P)+O_2$	$(3.2 \times 10^{-11}) \times \exp(70/T)$	4.1×10^{-11}	10
24.	$O(^1D)+H_2O \rightarrow 2OH$	2.2×10^{-10}	2.2×10^{-10}	10
25.	$OH+O(^3P) \rightarrow H+O_2$	$(2.2 \times 10^{-11}) \times \exp(120/T)$	3.3×10^{-11}	10
26.	$HO_2+H \rightarrow 2OH$ (90%) $\rightarrow H_2O+O(^1D)$ (2%) $\rightarrow H_2+O_2$ (8%)	8.1×10^{-11}	8.1×10^{-11}	10
27.	$2OH \rightarrow H_2O+O(^3P)$	$(4.2 \times 10^{-12}) \times \exp(-240/T)$	1.9×10^{-12}	10
28.	$H+O_2+M \rightarrow HO_2+M$	$k_0=(5.7 \times 10^{-32}) \times (T/300)^{-1.6}$ $k_\infty=7.5 \times 10^{-11}$	$k_0=5.9 \times 10^{-32}$ $k_\infty=7.5 \times 10^{-11}$	10
29.	$O(^3P)+H_2 \rightarrow OH+H$	4.11×10^{-18}	4.11×10^{-18}	10
30.	$2HO_2 \rightarrow H_2O_2+O_2$	$(2.3 \times 10^{-13}) \times \exp(600/T)$	1.8×10^{-12}	10

31.	$H_2O_2+OH \rightarrow H_2O+HO_2$	$(2.9 \times 10^{-12}) \times \exp(-160/T)$	1.7×10^{-12}	10
32.	$OH+HO_2 \rightarrow H_2O+O_2$	$(4.8 \times 10^{-11}) \times \exp(250/T)$	1.1×10^{-10}	10
33.	$O(^3P)+HO_2 \rightarrow OH+O_2$	$(3.0 \times 10^{-11}) \times \exp(200/T)$	5.9×10^{-11}	10
34.	$H_2O_2+O(^3P) \rightarrow OH+HO_2$	$(1.4 \times 10^{-12}) \times \exp(-2000/T)$	1.5×10^{-15}	10
35.	$OH+H_2 \rightarrow H_2O+H$	$(5.5 \times 10^{-12}) \times \exp(-2000/T)$	6.0×10^{-15}	10
36.	$OH+OH+M \rightarrow H_2O_2+M$	$k_0=(6.2 \times 10^{-31}) \times (T/300)^{-1}$ $k_\infty=2.6 \times 10^{-11}$	$k_0=6.3 \times 10^{-31}$ $k_\infty=2.6 \times 10^{-11}$	10
37.	$H_2O_2+h\nu \rightarrow 2OH$		8.6×10^{-6}	10
38.	$O(^1D)+H_2 \rightarrow OH+H$	1.1×10^{-10}	1.1×10^{-10}	10
39.	$O_3+h\nu \rightarrow O_2+O(^1D)$		1.0×10^{-5}	9,10
40.	$O_2+O(^3P) \rightarrow O_3$	$[M](6 \times 10^{-34})(T/300)^{-2.3}$	1.6×10^{-14}	10
41.	$O(^1D)+O_3 \rightarrow 2O_2$	1.2×10^{-10}	1.2×10^{-10}	10
42.	$O_3+O(^3P) \rightarrow 2O_2$	$(8 \times 10^{-12}) \times \exp(-2060/T)$	7.1×10^{-15}	10
43.	$H+O_3 \rightarrow OH+O_2$	$(1.4 \times 10^{-10}) \times \exp(-470/T)$	2.8×10^{-11}	10
44.	$O_3+OH \rightarrow HO_2+O_2$	$(1.6 \times 10^{-12}) \times \exp(-940/T)$	6.5×10^{-14}	10
45.	$O_3+HO_2 \rightarrow OH+2O_2$	$(1.1 \times 10^{-14}) \times \exp(-500/T)$	2.0×10^{-15}	10
46.	Uptake coefficient of OIO, I_2O_2		1	16
48.	Uptake coefficient of HI, HOI		0.03	2, 17
49.	Uptake coefficient of OH	$(1.2 \times 10^{-5}) \times \exp(1750/T)$	0.0047	2
49.	Uptake coefficient of HO_2	$(1.4 \times 10^{-8}) \times \exp(3780/T)$	0.0056	2

‡ Units: unimolecular reactions, s^{-1}; bimolecular reactions, cm^3 $molecule^{-1}$ s^{-1}; recombination reactions, cm^6 molecule $^{-2}$ s^{-1}, calculated using the formalism in *De More et al.* [1997], where $k=((k_0\,[M] / (1+ k_0\,[M]/k_\infty)) \times F_c^n)$, $F_c = 0.6$ and $n=\{1+(\log_{10}(k_0\,[M]/k_\infty))^2\}^{-1}$; photolysis rate constants, s^{-1}. 1.Calculated based on intensity of black-lights and cross section reported by *Mossinger et al*. [1998] (quantum yield=1) 2. *McFiggans et al*. [2000]; 3. *Sander et al.* [1986]; 4. *Cox et al*. [1999]; 5. *Atkinson et al*. [2000]. 6. Calculated based on intensity of black-lights and cross section reported by *Finlayson-Pitts and Pitts* [2000] (quantum yield=1); 7. Calculated based on intensity of black-lights and cross section reported by *Bloss et al.* [2001] (quantum yield=1); 8. Calculated based on intensity of black-lights and cross section reported by *Rowley et al*. [1999] (quantum yield=1); 9. Temperature and wavelength dependency of quantum yield obtained from *Finlayson-Pitts and Pitts* [2000]; 10. *De More et al*. [1997]; 11. OIO photolysis yields from *Ashworth et al.* [2002]. 12. OIO cross section from *Bloss et al.* [2001]. 13a. *McFiggans* [2001]. 13b. $J_{I2O2}=0.2*J_{IO}$ (*McFiggans* [2001]). 14. *Vikis and MacFarlane* [1985] 15. *Burkholder* [2001], *Sander* [2002]. 16. Based on calculations from chamber experiments; See text. 17. *Percival et al.* [1999]; *Mossinger et al.* [2001]; *Holmes et al.* [2001].

Table 3.3. Summary of chemical kinetics simulations performed as direct comparison to the experiments and as parametric studies of the base case

								AEROSOL MOLE FRACTIONS [c]				
Simulation	Simulation Objective	Initial CH_2I_2 (ppb)	Initial O_3 (ppb)	RH (%)	UV light Intens.	Time scale (min) [a]	O_3 destr. (ppb)	OIO	I_2O_2	HOI	HI	HO_x [b]
	Simulations Performed As Direct Comparison to the Experiments											
S 1	Compare to E1	5	100	2	1	25	39.9	0.993	3.91E-03	2.77E-03	1.93E-07	6.59E-06
S 2	Compare to E2	5	100	65	1	17	29.3	0.939	3.38E-03	0.058	3.91E-06	1.38E-04
S 3	Compare to E3	0.5	100	2	1	37	7.1	0.97	9.30E-04	0.028	3.07E-05	1.08E-03
S 4	Compare to E4	0.05	100	2	1	100	2.8	0.797	5.51E-04	0.152	7.20E-04	0.051
S 5	Compare to E5	0.015	100	2	1	624	11	0.596	3.17E-04	0.207	1.80E-03	0.195
S 6	Compare to E6	50	500	2	1	9.5	309	0.984	0.016	4.89E-04	3.28E-09	1.81E-07
	Simulations Performed as Parametric Studies of the Base Case											
S 7	Low CH_2I_2 + Marine + Chamber Lights	0.001	30	76	1	964	16.8	4.08E-03	2.96E-06	0.068	5.69E-04	0.928
S 8	Low CH_2I_2 + Marine + Solar Light	0.001	30	76	Zenith 30	1482	29	1.99E-04	2.15E-06	0.044	8.31E-04	0.955
S 9	Effect of Humidity	50	500	65	1	9	306	0.971	1.58E-02	0.013	8.87E-08	4.97E-06
S 10	Effect of Humidity	0.5	100	65	1	35	12.2	0.705	1.04E-03	0.282	9.59E-05	0.013
S 11	Effect of Humidity	0.05	100	65	1	127	11	0.3	3.75E-04	0.474	5.32E-04	0.225
S 12	Effect of Humidity	0.015	100	65	1	820	49.9	0.12	1.09E-04	0.383	7.90E-04	0.496
S 13	Solar Light	5	500	2	Zenith 30	11.5	394	0.981	0.012	6.61E-03	1.71E-06	1.42E-05
S 14	Effect of O_3 Concentration	5	70	2	1	33.5	36.3	0.993	4.29E-03	2.43E-03	1.69E-07	4.86E-06
S 15	Effect of O_3 Concentration	5	150	2	1	19.5	49.5	0.993	3.44E-03	3.30E-03	2.29E-07	9.65E-06
S 16	Effect of Radiation Intensity	5	100	2	0.25	31	29.2	0.995	3.41E-03	1.20E-03	1.67E-08	2.08E-06
S 17	Effect of Radiation Intensity	5	100	2	2	25.5	45.6	0.991	4.44E-03	5.02E-03	1.04E-06	1.79E-05
S 18	Effect of Aerosol Surface Area	50	500	2	1	19	461.3	0.996	3.29E-03	4.72E-04	4.78E-09	5.30E-08
S 19	Effect of Aerosol Surface Area	0.05	100	2	1	23	0.5	0.709	2.46E-03	0.195	2.73E-04	0.093
S 20	Effect of Aerosol Surface Area	0.015	100	2	1	27	0.4	0.269	8.92E-04	0.234	4.15E-04	0.496

[a] Defined as the time at which 1 - 1/e (~63%) of the initial iodine atoms are in the aerosol phase. [b] The large amount of HO_x predicted to be in the aerosol phase in some simulations suggests that the constant uptake coefficients assumed for these species may not be appropriate for very low aerosol concentrations. [c] Aerosol mole fractions when 95% of the I atoms in the system are in the aerosol phase except for S8 where 75% of I atoms are in the aerosol phase

Table 3.4. Summary of chemical kinetics simulations performed as tests of alternative mechanisms for the gas-phase chemical kinetics, different aerosol uptake parameters, or with solar light instead of chamber light (blacklights)

								AEROSOL MOLE FRACTIONS							
Simulation	Simulation Objective	Initial CH_2I_2 (ppb)	Initial O_3 (ppb)	RH (%)	UV light Intens.	Time scale (min)	O_3 destr. (ppb)	OIO	I_2O_2	HOI	HI	HO_x	$(OIO)_2$	I_2	HIO_3
	Simulations Performed as Tests of Alternative Gas and Aerosol Uptake Mechanisms														
S 21	I_2O_2->2I+O_2	5	100	2	1	33	70.5	0.993	4.26E-03	2.80E-03	2.12E-07	5.19E-06			
S 22	No I_2O_2 Thermolysis	5	100	2	1	21	46.1	0.703	2.94E-01	2.27E-03	1.63E-07	4.99E-06			
S 23	Unity Aerosol Uptake Coeff. HOI & HI	5	100	2	1	25.5	38.5	0.993	3.91E-03	2.93E-03	9.00E-08	2.61E-06			
S 24	I_2 taken up by aerosol (α=1)	50	500	2	1	3.25	140	0.502	1.49E-03	1.10E-04	8.76E-09	1.01E-06		4.97E-01	
S 25	I_2 taken up by aerosol (α=1)	5	100	2	1	7.25	14.5	0.273	1.34E-04	1.36E-04	7.00E-09	1.28E-06		7.26E-01	
S 26	I_2 taken up by aerosol (α=1)	0.5	100	2	1	17	3.45	0.337	1.57E-04	2.98E-03	1.61E-06	1.32E-04		6.60E-01	
S 27	I_2 taken up by aerosol (α=1)	0.05	100	2	1	57	1.6	0.365	2.02E-04	6.25E-02	3.56E-04	2.33E-02		5.49E-01	
S 28	I_2 taken up by aerosol (α=1)	0.015	100	2	1	192	6.05	0.302	1.68E-04	1.16E-01	1.08E-03	1.28E-01		4.52E-01	
S 29	ϕ (OIO)=15%	50	500	2	1	7.5	265	0.986	1.35E-02	4.84E-04	3.35E-09	2.26E-07			
S 30	ϕ (OIO)=15%	5	100	2	1	18	29.9	0.995	2.60E-03	2.45E-03	1.85E-07	6.81E-06			
S 31	ϕ (OIO)=15%	0.5	100	2	1	23.5	4	0.983	3.53E-04	1.60E-02	1.78E-05	7.96E-04			
S 32	ϕ (OIO)=15%	0.05	100	2	1	74	1.9	0.876	2.32E-04	8.89E-02	4.64E-04	3.45E-02			
S 33	ϕ (OIO)=15%	0.015	100	2	1	442	6.85	0.775	1.36E-04	1.08E-01	9.55E-04	1.16E-01			
S 34	2 OIO-> $(OIO)_2$	50	500	2	1	7.5	265	0.754	1.67E-02	5.98E-04	4.41E-09	2.80E-07	2.29E-01		
S 35	2 OIO-> $(OIO)_2$	5	100	2	1	19.5	31.05	0.793	3.51E-03	3.10E-03	2.36E-07	8.41E-06	2.01E-01		
S 36	2 OIO-> $(OIO)_2$	0.5	100	2	1	29.5	5.4	0.747	7.74E-04	2.89E-02	3.47E-05	1.27E-03	2.22E-01		
S 37	2 OIO-> $(OIO)_2$	0.05	100	2	1	94	2.6	0.721	5.05E-04	1.50E-01	7.40E-04	5.29E-02	7.53E-02		
S 38	2 OIO-> $(OIO)_2$	0.015	100	2	1	298	10.6	0.548	2.91E-04	2.04E-01	1.81E-03	2.02E-01	4.45E-02		
S 39	CH_2I Rxns (1/10 Coll rate)	5	100	2	1	25.5	38.8	0.993	3.91E-03	2.78E-03	1.94E-07	6.61E-06			
S 40	CH_2I Rxns (1/1000 Coll rate)	5	100	2	1	25.5	37.5	0.993	3.94E-03	2.92E-03	2.21E-07	7.79E-06			
S 41	OIO + I -> I_2O_2	5	100	2	1	36	39.3	0.987	9.08E-03	3.63E-03	2.23E-07	7.60E-07			
S 42	OIO + I -> I_2 + O_2	5	100	2	1	46	53.9	0.988	7.75E-03	4.00E-03	2.44E-07	7.40E-06			
S 43	OIO + OH -> HIO_3 -> aerosol	5	100	2	1	25.5	38.9	0.994	3.90E-03	2.48E-03	1.80E-07	6.30E-06			2.88E-04
S 44	OIO + OH -> HIO_3 -> aerosol	5	100	65	1	17.5	29.25	0.938	3.40E-03	5.40E-02	3.82E-06	6.84E-05			4.91E-03

Table 3.5. Summary of the effects of variations of the rates and structure of the kinetic mechanism on the agreement between experiments and simulations, and on the major predicted aerosol species. For the first two columns, grayed cells indicate increased discrepancy, and boxed cells increased agreement with the experiments. The meaning of the arrows is as follows: ↑ means that the modification of the mechanism described in the first column of that row results in an increase on the model result described on the top of that column. ↑↑ indicates a very large increase, ↓ a decrease, and ↔ minor or no change.

Mechanism Modification	**Effect on Gas-to-Particle Time Scale**	**Effect on O_3 Consumption**	**Effect on Aerosol OIO**	**Effect on Aerosol HOI**	**Effect on other Aerosol Species**
	Need ↑ to match exp.	**Need ↓ to match exp.**			
(a1) I_2O_2 thermolysis to I instead of IO	↑	↑↑	↔	↔	↔
(a2) No I_2O_2 thermolysis	↔	↑	↓	↔	↑↑ I_2O_2
(b) Faster aerosol uptake of HOI & HI	↔	↔	↔	↔	↔
(c) Uptake of I_2	↓	↓	↓	↔	↑↑ I_2
(d) ϕ(OIO) = 0.15	↓	↓	↑	↓	
(e) OIO dimerization and dimer uptake	↓	↓	↔	↔	
(f) Slower release of 2nd I atom from CH_2I_2	↔	↔	↔	↔	↔
(g1) OIO + I → I_2O_2	↑	↔	↔	↔	
(g2) OIO + I → I_2 + O_2	↑	↑	↔	↔	
(h) OIO + OH → HIO_3	↔	↔	↔	↔	↑ HIO_3

Table 3.6. Synthesis of evidence on aerosol composition and identity of nucleating species

Source of Information	**Nucleating and/or aerosol species**
Lack of Nucleation when O_3 not present + Kinetic Simulations	• I and I_2 are not the nucleating species
Chemical simulations	• OIO at high concentrations • HOI and OIO at low concentrations
Experimental nucleation delay	• OIO, IO, and I_2O could be involved in nucleation • HOI is less likely to be involved • I_2O_2 and HI are not involved
AMS	• I_xO_y and either/both H_2O/HIO_3
Crystalline structure and speed of nucleation	• More likely I_2O_4 or I_2O_5 • Less likely I_2O_6
Lack of hygroscopic growth in HTDMA	• Most likely I_2O_4 • Not likely I_2O_5 and/or I_4O_9
SUMMARY	• **OIO most likely responsible for nucleation** • **I_2O_4 most likely dominant aerosol species**

Figure 3.1. Evolution of the number, volume, and mass concentrations in the chamber as a function of time after inception of photolysis for the base case experiment (E1: 5 ppb CH_2I_2, 100 ppb O_3, <2% RH). Three measurements of the particle number concentration, for instruments with different response cutoff for smaller particles are included. The processes estimated to contribute to the aerosol dynamics at each instant of time are indicated above the graph.

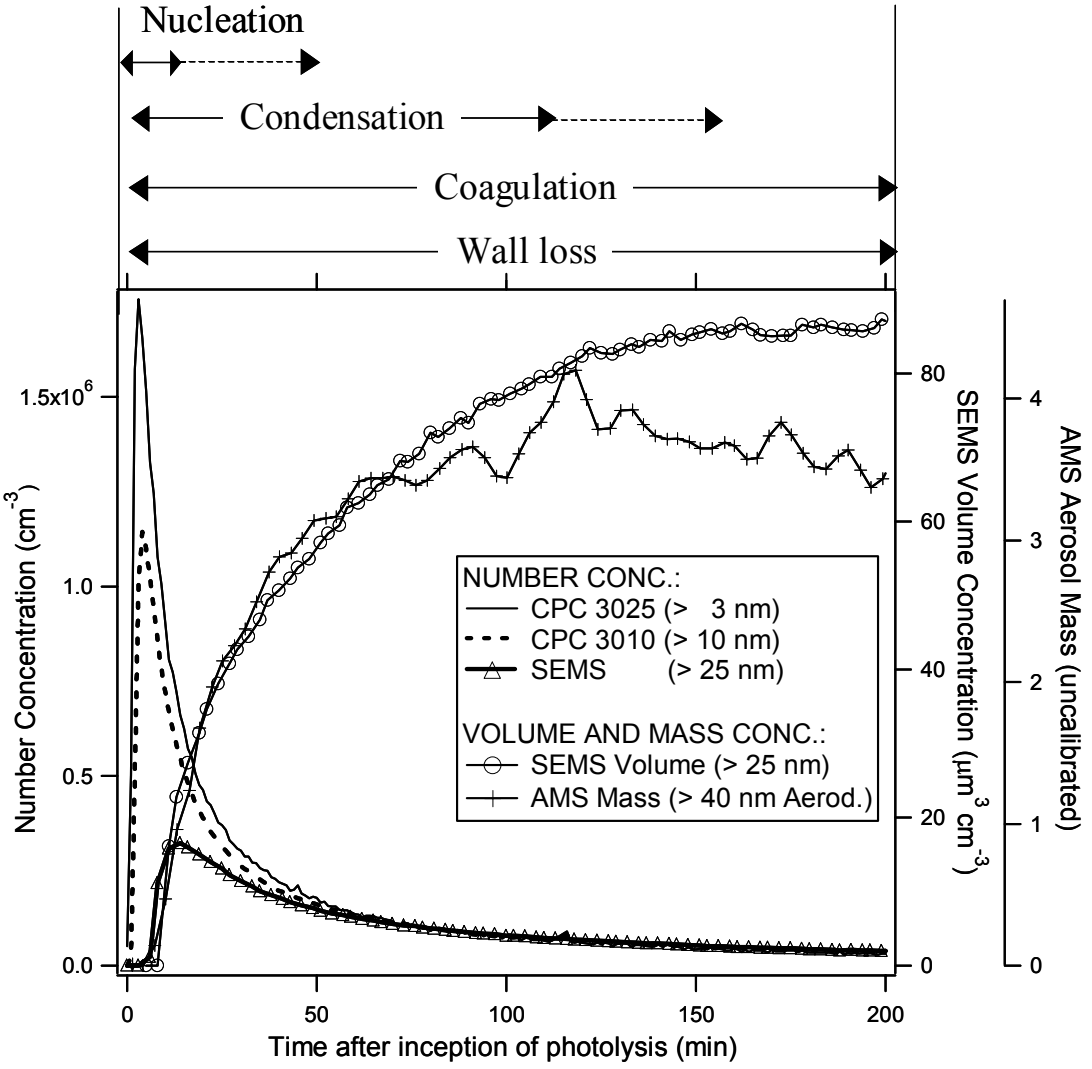

Figure 3.2. Evolution of the number, volume, and mass concentrations in the chamber during the initial minutes after inception of photolysis for the base case experiment (E1: 5 ppb CH_2I_2, 100 ppb O_3, <2% RH)

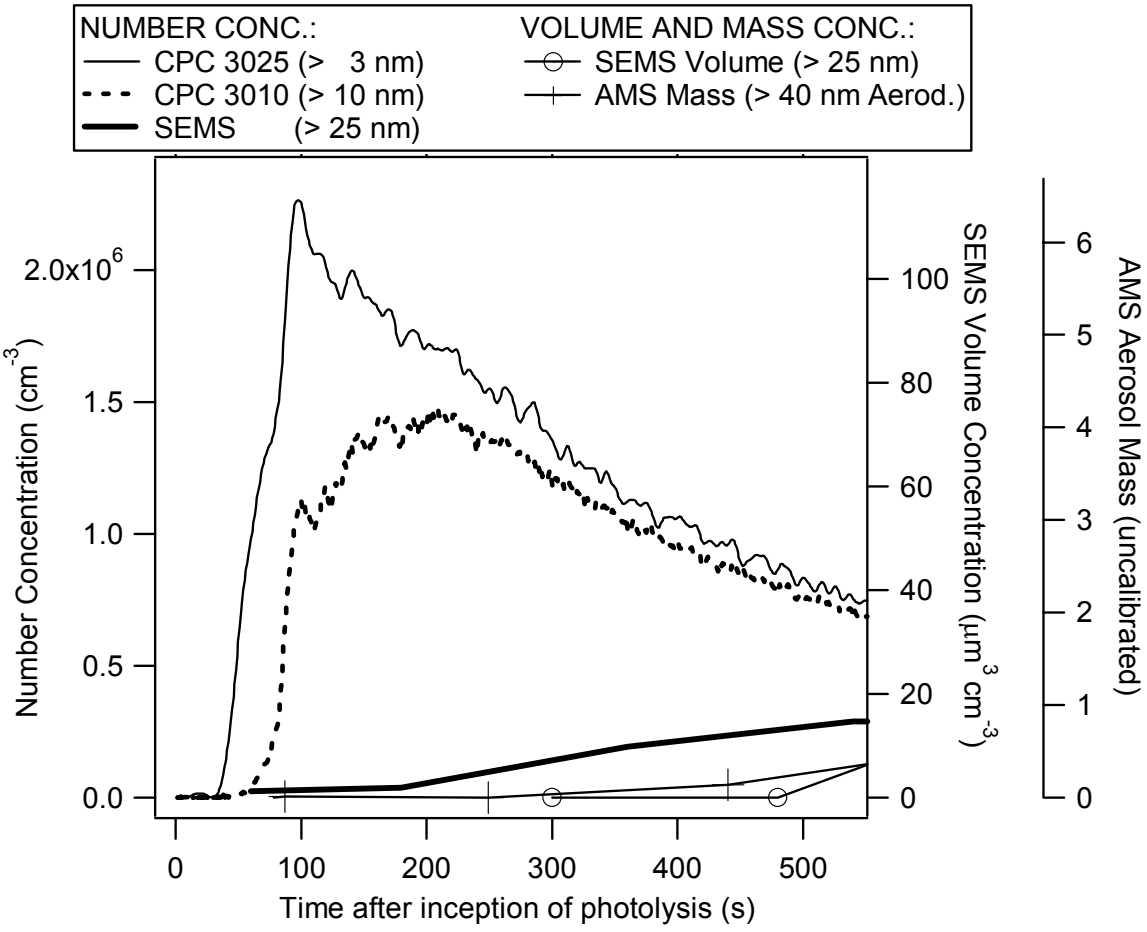

Figure 3.3. SEMS Size distributions at different times during the base case experiment (E1: 5 ppb CH_2I_2, 100 ppb O_3, <2% RH). Particles grow into the SEMS range due to condensation on / coagulation of the nucleation-mode particles. Later on, nucleation stops, and the number of particles decreases as their size increases due to the combined effects of condensation, coagulation, and wall loss. The concentrations for the smallest particles are unrealistically low during nucleation because the SEMS as configured in this study detects these particles inefficiently.

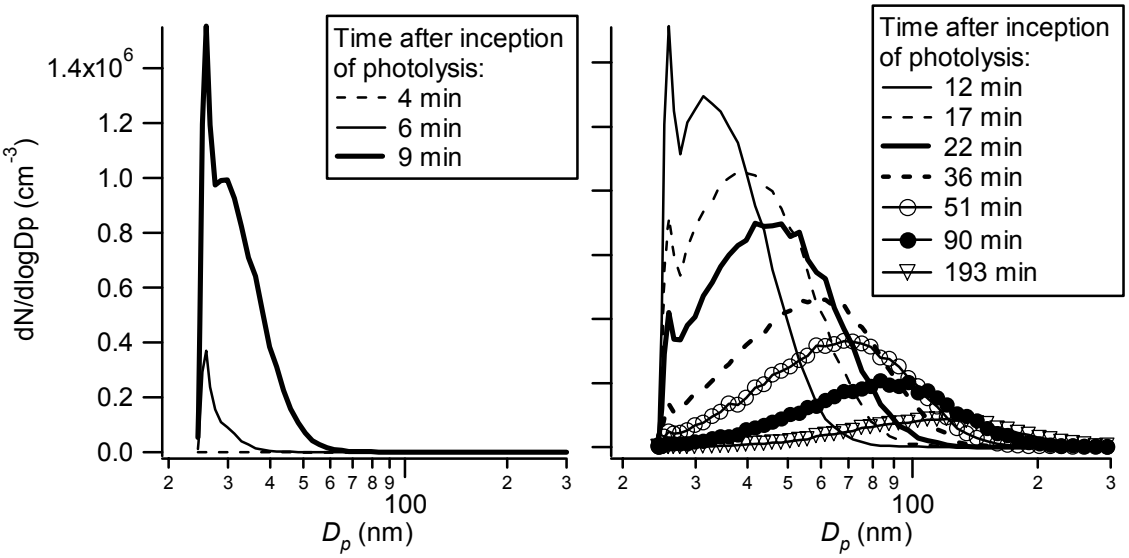

Figure 3.4. Comparison of the volume size distributions measured by the SEMS with the mass distributions measured by the AMS for two times during the base case experiment (E1: 5 ppb CH_2I_2, 100 ppb O_3, <2% RH)

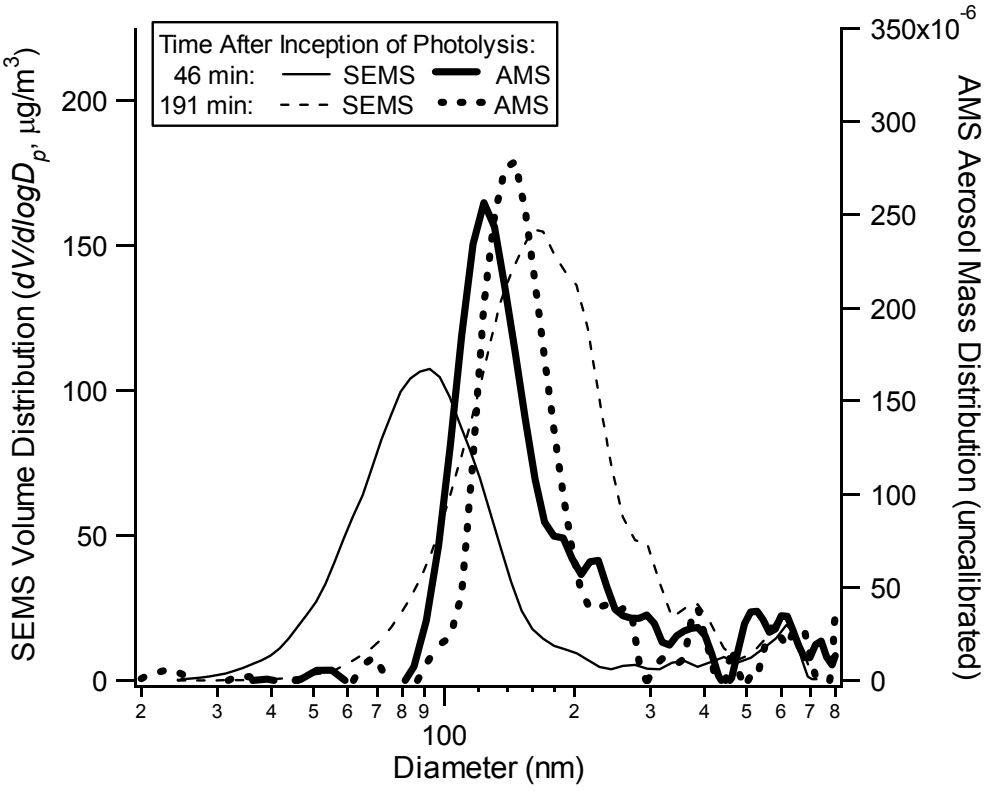

Figure 3.5. Comparison of the maximum experimental particle number, area, and volume concentrations measured in the chamber as a function of initial CH_2I_2 mixing ratio

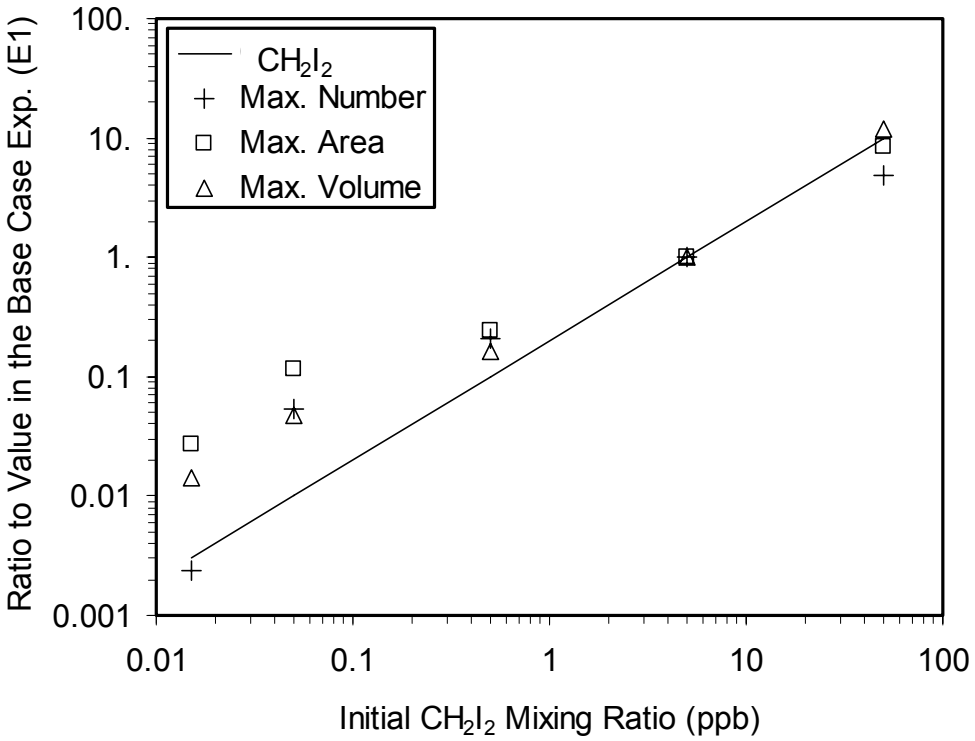

Figure 3.6. Observed time scales of gas-to-particle conversion as a function of initial CH_2I_2 mixing ratio: delay to nucleation, time from nucleation to particle number peak, and particle volume increase. The e-folding time scale of iodine gas-to-particle conversion simulated by the numerical model of section 3.5 is also shown here.

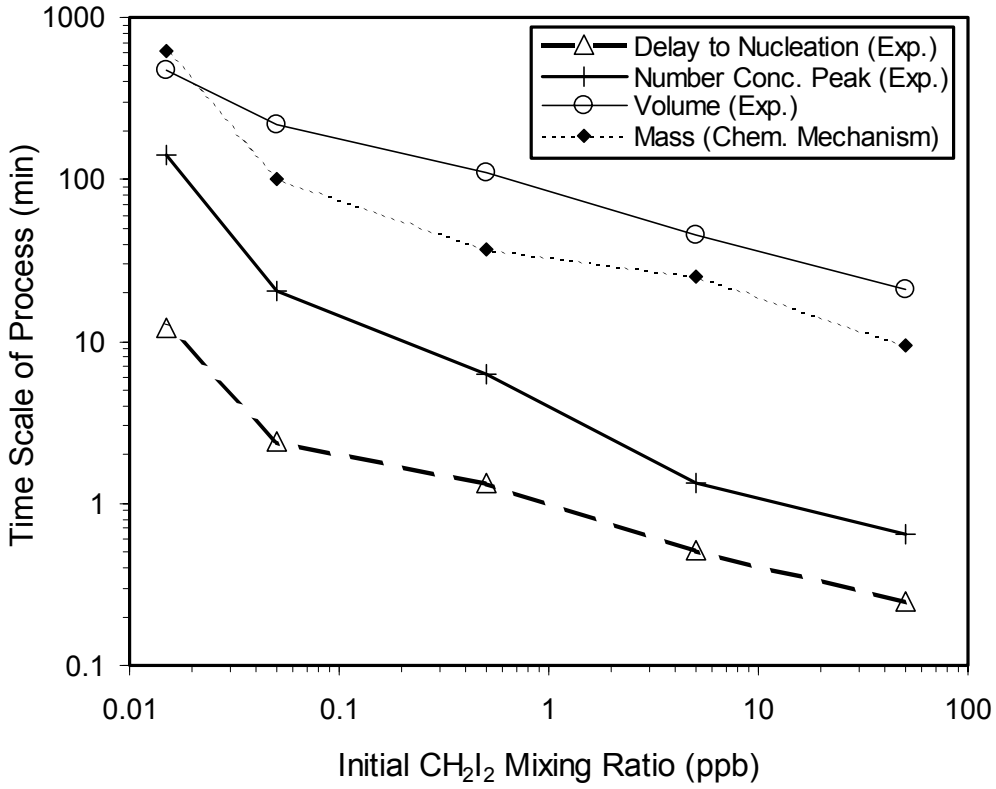

Figure 3.7. Hygroscopic growth factor determined by the Hygroscopicity Tandem Differential Mobility Analyzer (HTDMA) as a function of relative humidity for experiments E1 and E2 (RH <2% and 65% respectively; 5 ppb CH_2I_2, 100 ppb O_3). In this experiment, particles are size selected by the first DMA at the humidity of the chamber, allowed to equilibrate at a different relative humidity, and size classified by the second DMA. The ratio of the final to initial diameters is the hygroscopic growth factor.

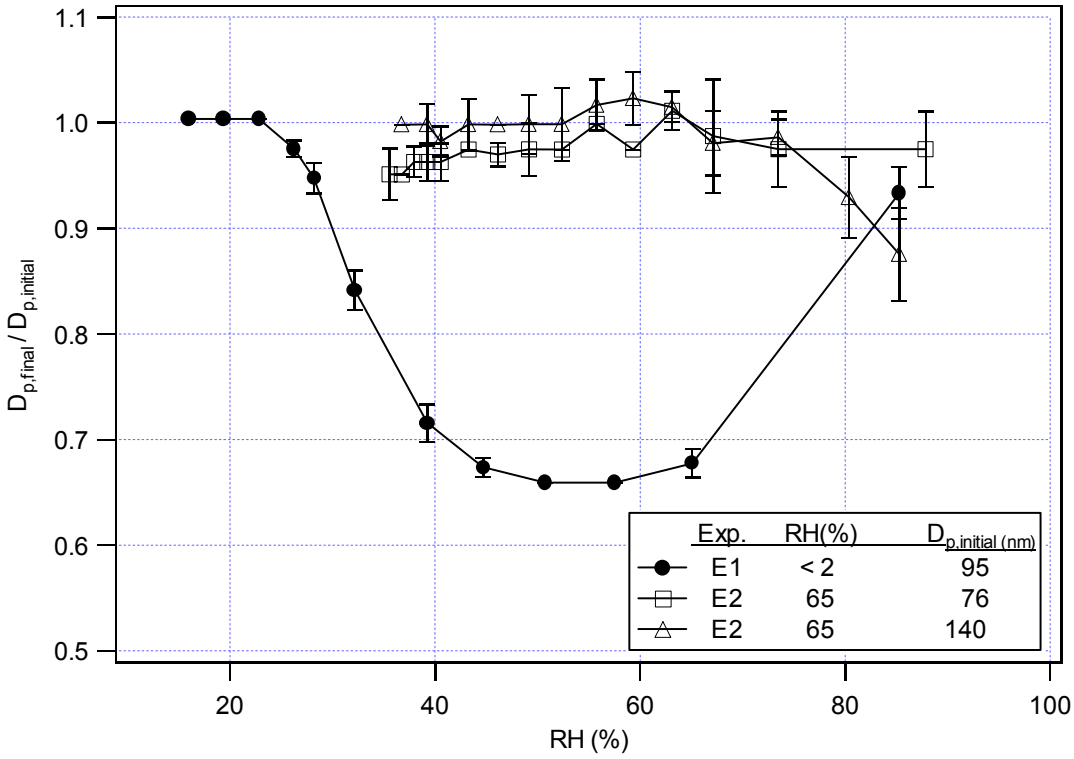

Figure 3.8. Total aerosol mass spectrum measured with the Aerodyne AMS for experiment E6 (50 ppb CH_2I_2, 500 ppb O_3, <2% RH). In the AMS, the particles are evaporated on a heated molybdenum surface (600°C) under high vacuum (10^{-7} Torr), followed by 70 eV electron ionization (see text).

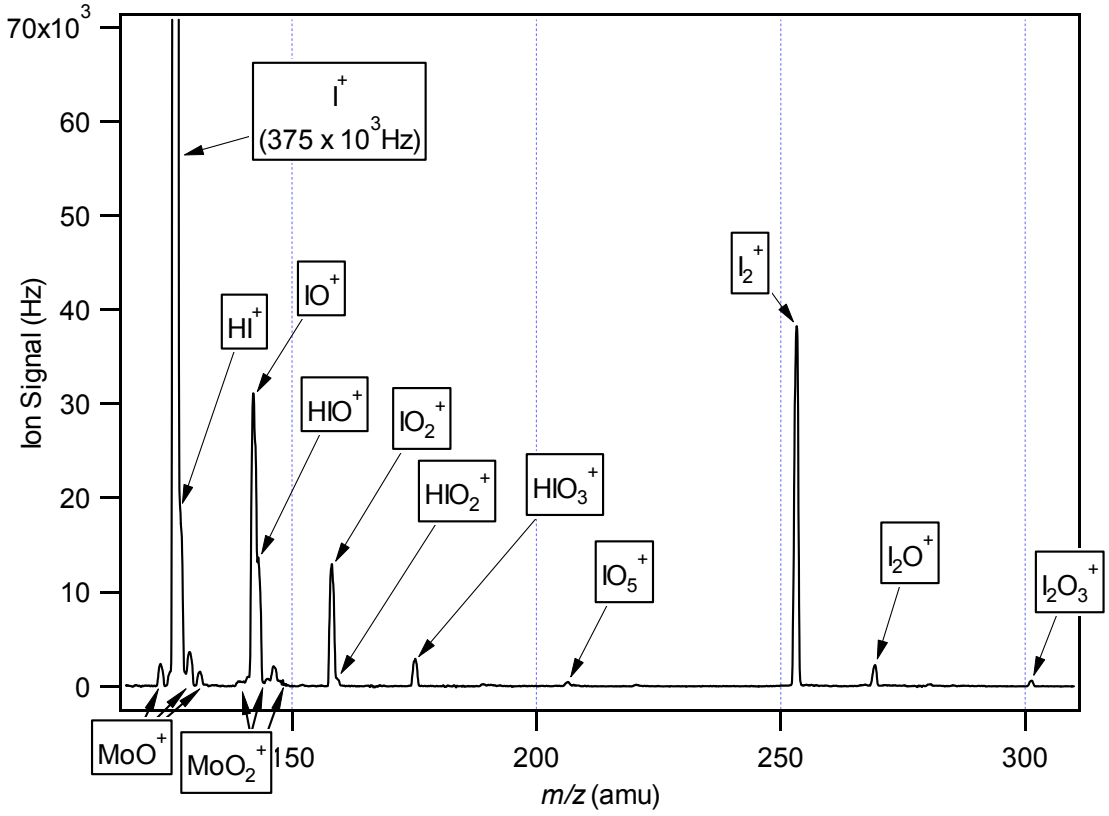

Figure 3.9. Calculated variation of the mobility diameter, vacuum aerodynamic diameter, and effective density (D_{va}/D_m) for a particle with a volume equivalent diameter (D_v) of 100 nm as a function of the dynamic shape factor χ (assuming $\chi = \chi_v$) for particles of unit material density (ρ_p = 1 g cm^{-3})

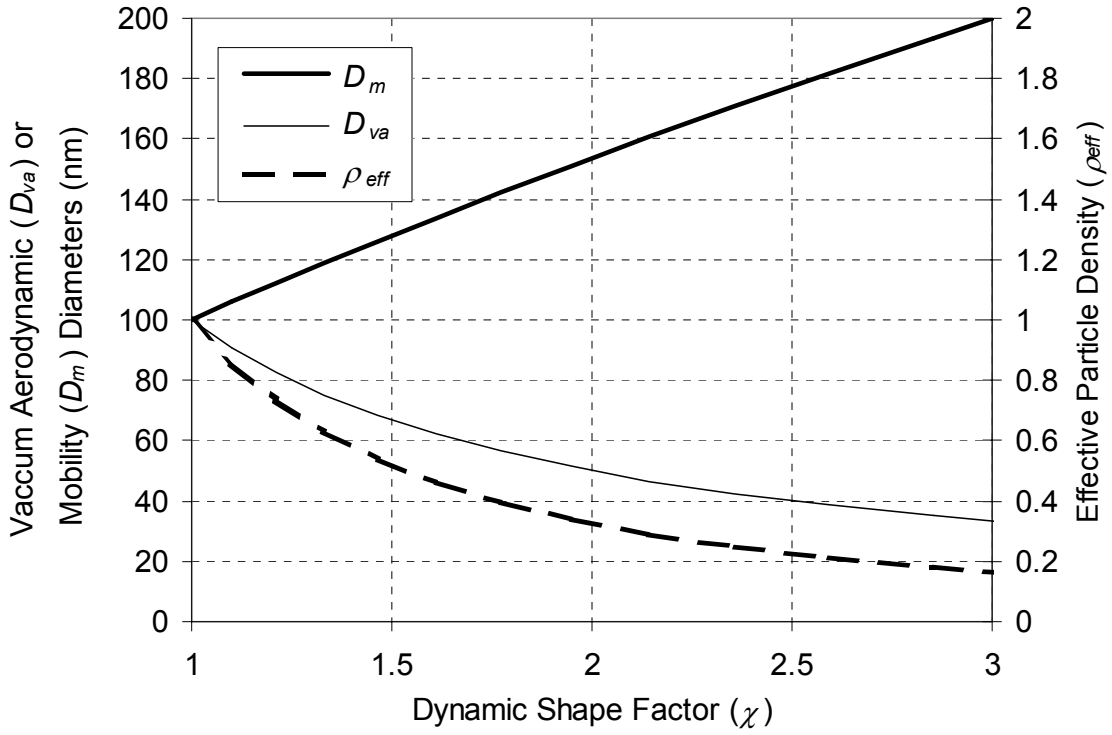

Figure 3.10. Comparison of the measured size distributions during the base case experiment (E1: 5 ppb CH_2I_2, 100 ppb O_3, <2% RH) with the theoretical self-preserving distributions during coagulation in the free molecular regime as a function of mass fractal dimension D_f

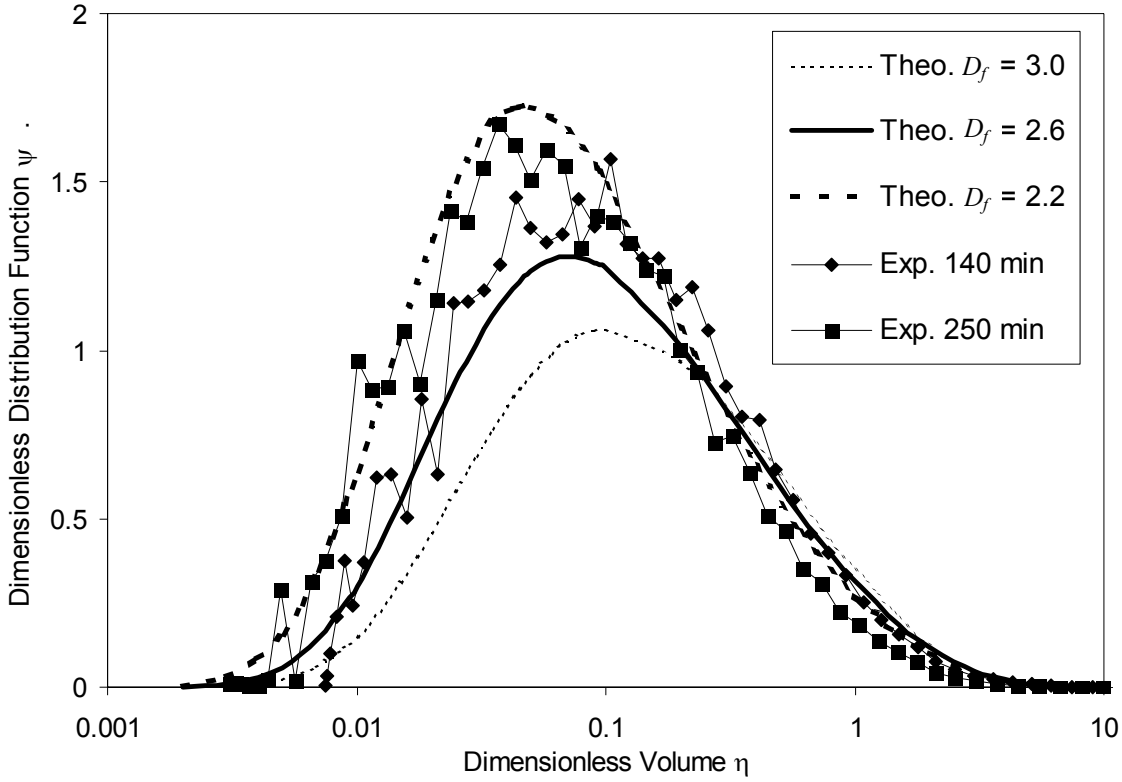

Figure 3.11. Theoretical decay of particle number concentrations as a function of the mass fractal dimension D_f, compared with the experimental decays for experiments E1 and E2 (RH <2% and 65% respectively; 5 ppb CH_2I_2, 100 ppb O_3).

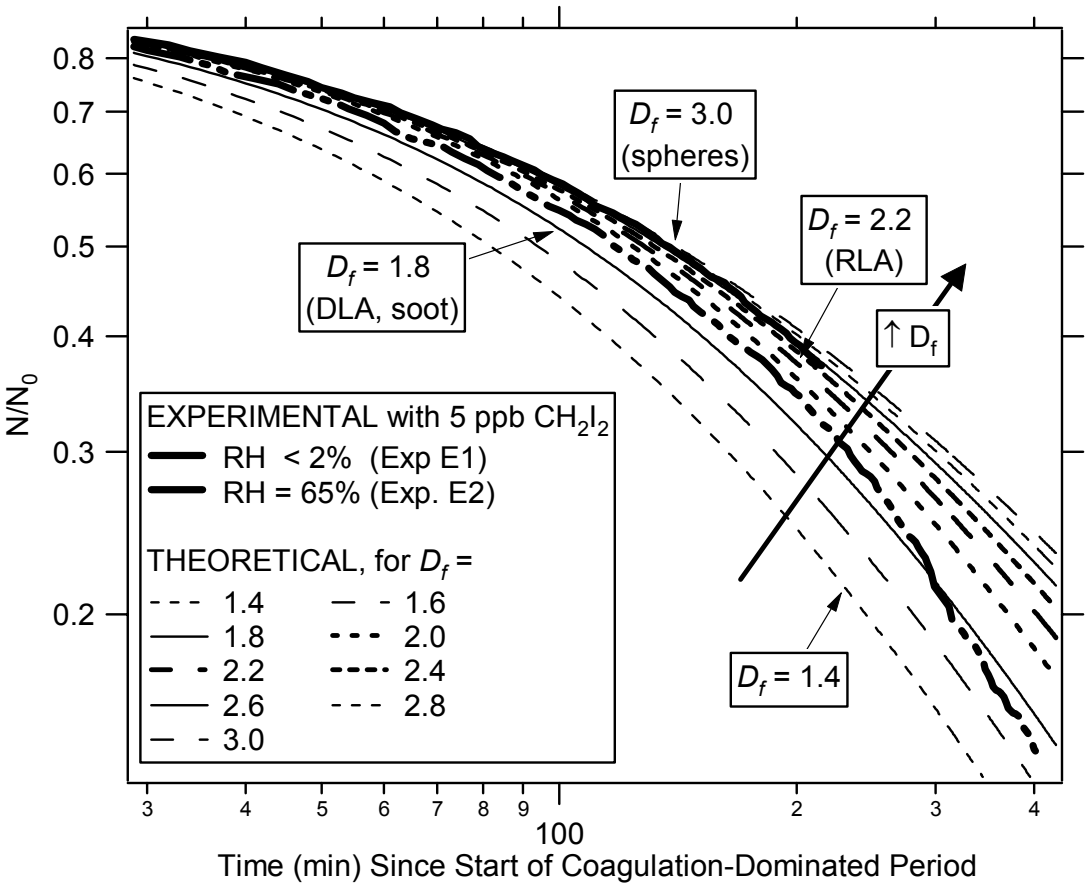

Figure 3.12. Schematic representation of the chemical mechanism used in the gas-phase and aerosol uptake simulations. For clarity, only the reactions that involve iodine species and play a significant role in any of the simulations are included in this schematic.

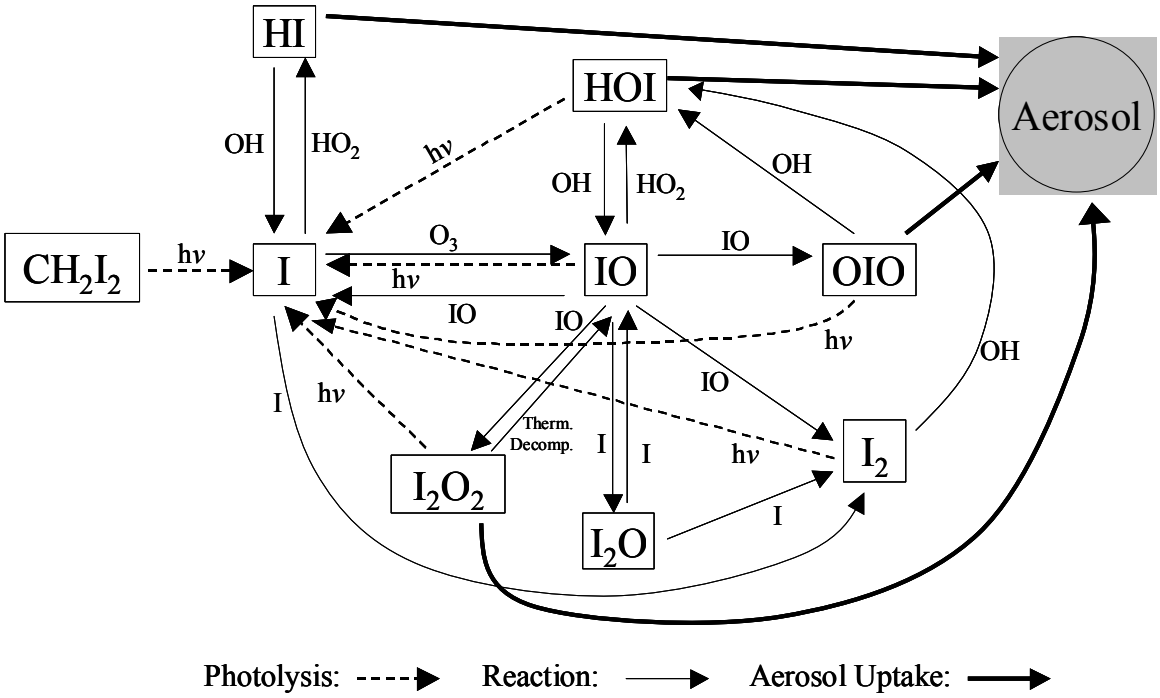

Figure 3.13. Simulated concentration profiles of the main iodine species for the simulation base case S1 (5 ppb CH_2I_2, 100 ppb O_3, 2% RH), which corresponds to the conditions of the experimental base case E1. This is a stacked plot: the vertical extent of each band represents the mixing ratio of each species (as iodine atoms) at a given time, and the total number of iodine atoms in the system remain constant. Concentrations of the species not in the legend are too small to be seen in the graph.

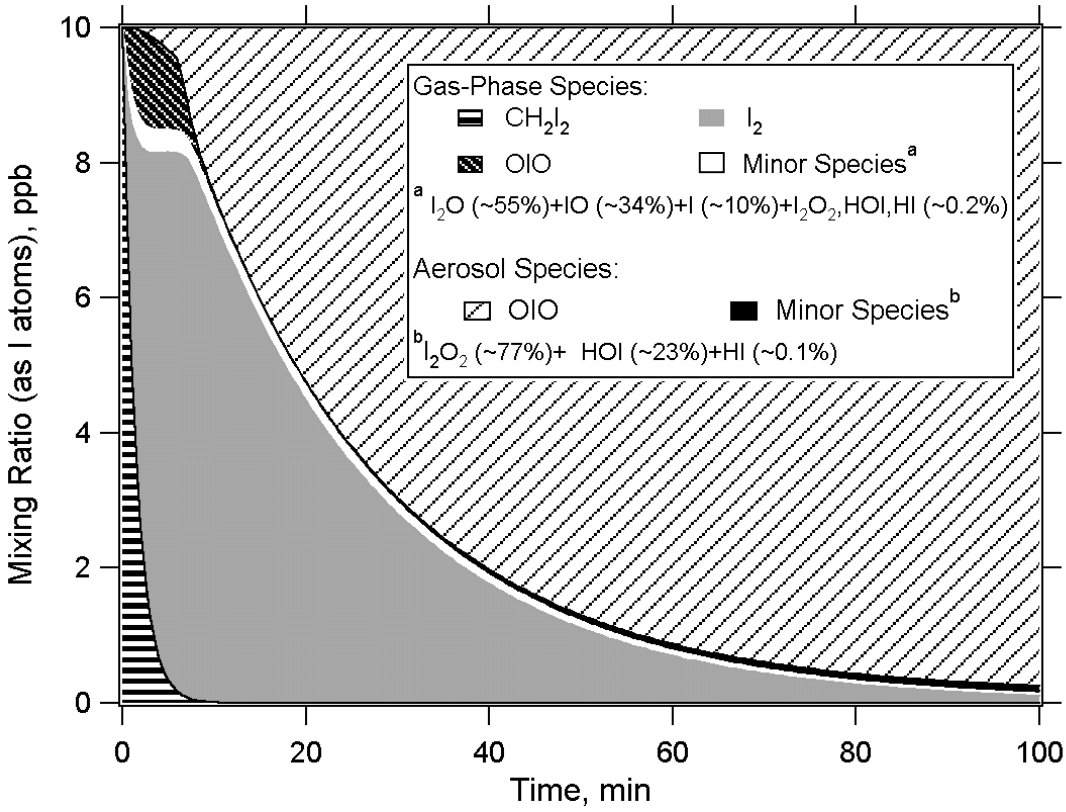

Figure 3.14. Mixing ratios (i.e., mole fraction) of the aerosol species predicted by the simulation mechanism as a function of initial CH_2I_2 concentration, at the time in each simulation when 95% of initial iodine is in the aerosol phase

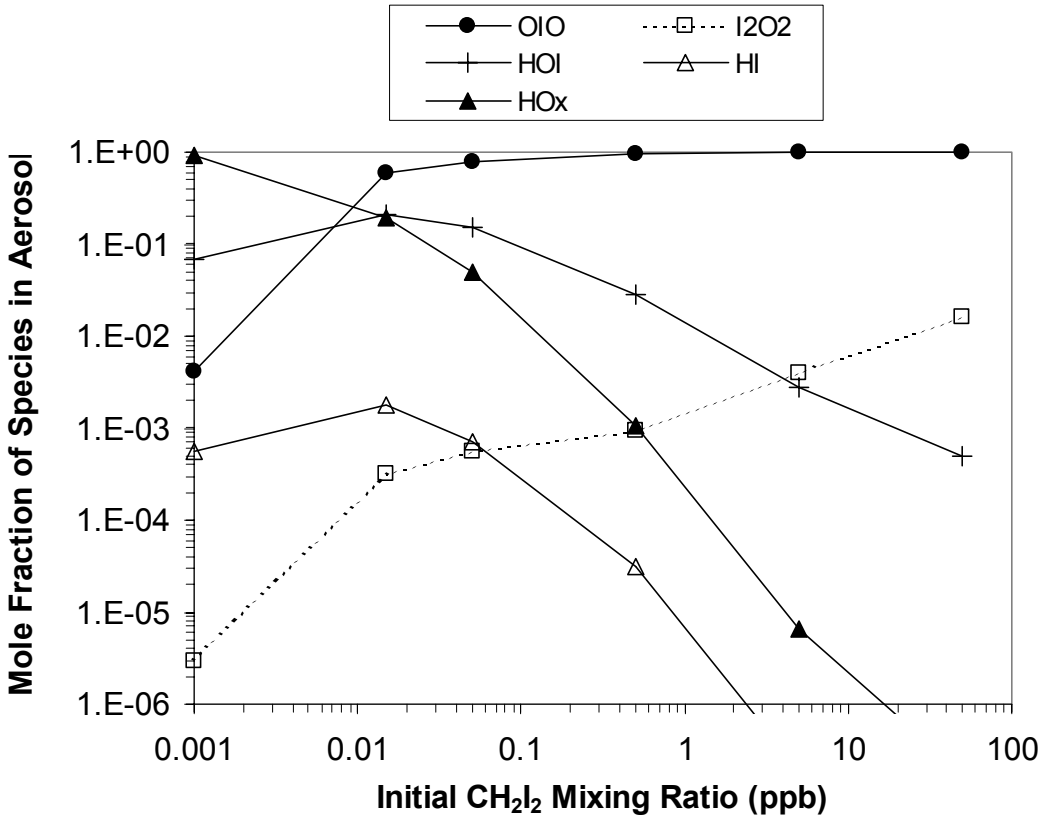

Figure 3.15. Comparison of the observed and predicted O_3 concentrations evolution as a function of time since inception of photolysis for the base case (cases E1 and S1)

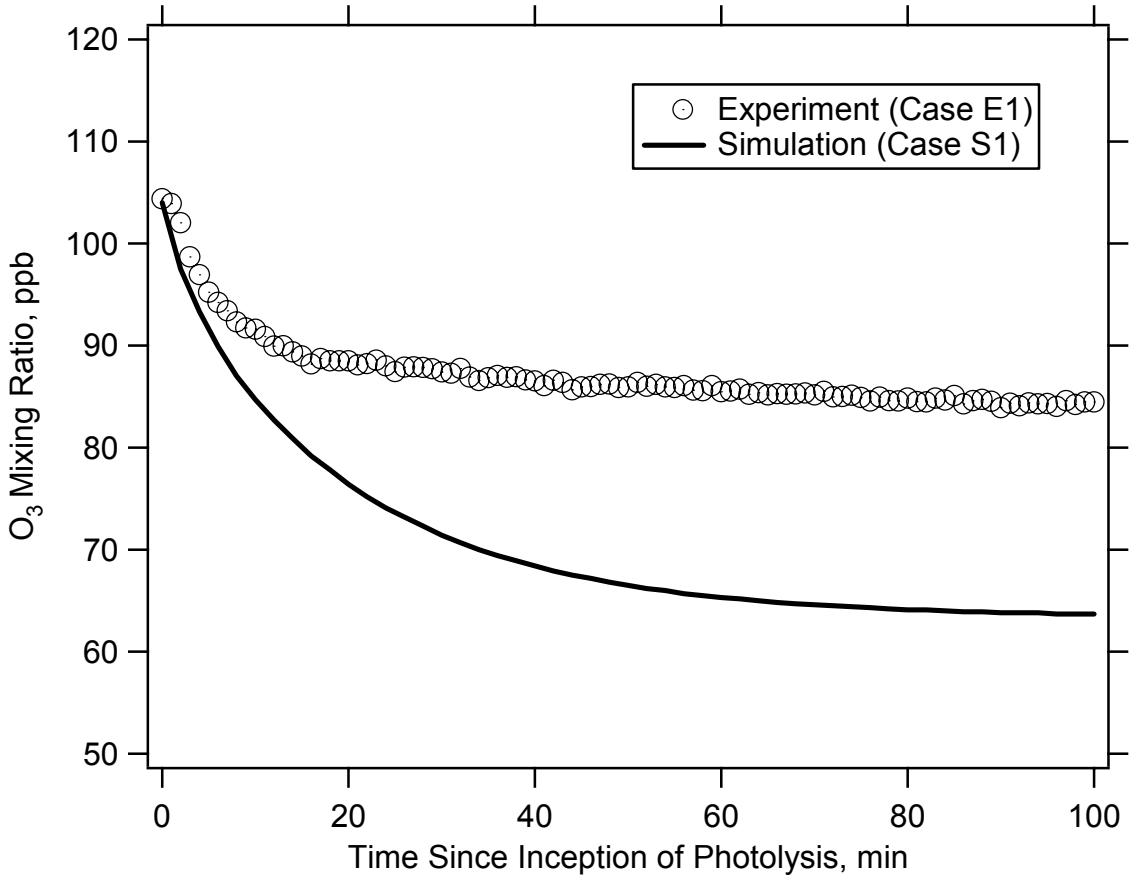

Figure 3.16. Predicted gas-phase concentrations at the inception of the experimental nucleation burst, as a function of initial CH_2I_2 mixing ratio. The y-axis has been limited to about six orders of magnitude below the concentration of the major species. Also shown are the minimum concentrations needed for nucleation at ambient conditions for the H_2SO_4-H_2O and H_2SO_4-NH_3-H_2O systems (see text).